RESEARCH ARTICLE

VOLCANICA

Reconstruction of the 29th December 2013 eruption of San Miguel volcano, El Salvador, using video, photographs, and pyroclastic deposits

Richard J. Brown*[α], Walter Hernández[†β], Demetrio Escobar[β], Eduardo Gutiérrez[‡β], Julia M. Crummy[γ], Rosemary P. Cole[δ], and Pierre-Yves Tournigand[ε]

[α] Department of Earth Sciences, Durham University, Durham, DH1 3LE, UK.
[β] Ministerio de Medio Ambiente y Recursos Naturales (MARN), Calle y Colonia Las Mercedes, San Salvador, El Salvador.
[γ] British Geological Survey, The Lyell Centre, Edinburgh, Research Avenue South, EH14 4AP, Scotland, UK.
[δ] Institute of Earth Sciences, Sturlugata 7 - Askja, 101 Reykjavík, Iceland.
[ε] Physical Geography, Department of Geography, Vrije Universiteit Brussel, Brussels, Belgium.

Abstract

San Miguel (or Chaparrastique) volcano, El Salvador, erupted on the 29th December 2013, after almost 40 years of quiescence. Initial vent-clearing explosions ejected ballistic blocks and produced a pyroclastic density current (PDC) that flowed down the upper flanks. Plume ascent speeds peaked at 50–70 m s^{-1} and declined over time. The main phase of the volcanic explosivity index (VEI) 2 eruption produced a sub-Plinian plume that dispersed 10^6 m^3 ash >20,000 km^2 across El Salvador in to Honduras. Plume structure was complex due to strong wind shear and to contributions from co-PDC ash. Tephra fall deposits dispersed westwards include a basal white ash layer of ash-coated clasts and ash aggregates, a grey fine ash co-PDC layer, and a layer of coarse ash to fine lapilli-grade scoria. The eruption provides a useful case study to understand the range of volcanic activity at the volcano.

Ágrip

El volcán San Miguel, El Salvador, entró en erupción el 29 de diciembre de 2013, después de casi 40 años de calma. Las explosiones iniciales limpiaron el cráter, expulsaron bloques balísticos y produjeron una corriente piroclástica densa (CPD) que fluyeron por los flancos superiores. Las velocidades de la pluma alcanzaron un máximo de 50–70 m s^{-1} y disminuyeron con el tiempo. La fase principal de la erupción VEI 2 produjo una pluma subpliniana que dispersó 10^6 m^3 de cenizas >20, 000 km^2 a través de El Salvador hasta Honduras. La estructura de la pluma era compleja debido a la dirección del viento predominante y a los aportes de las cenizas co-CPD. Las tefras de caída que se dispersaron hacia el oeste incluyen una capa basal de ceniza blanca con clastos recubiertos de ceniza y agregados de ceniza, una capa de ceniza fina gris co-CPD y una capa de ceniza gruesa a escoria fina de tamaño lapilli. La erupción proporciona un caso de estudio útil para comprender el rango de actividad volcánica del volcán.

Keywords: San Miguel; El Salvador; Tephra fall; Pyroclastic density current; Explosive eruption; VEI2.

1 Introduction

Small explosive eruptions—i.e. ~10^6 m^3 of tephra; volcanic explosivity index (VEI)2 of Newhall and Self [1982]—account for nearly 50 % of all recorded eruptions [Siebert et al. 2015]. They present a similar range of hazards to larger eruptions (VEI >4) such as ballistic bombs, tephra fall, pyroclastic density currents, gas emissions, earthquakes, and lahars [Brown et al. 2015]. The tephra fall deposits are commonly thin, weakly dispersed, and—following deposition—are subject to a host of deleterious surface processes and to anthropogenic and biological activity that can rapidly remove them from the geological record. Preservation of tephra is dependent on slope angle, vegetation cover, altitude and climate [e.g. Collins et al. 1983; Collins and Dunne 1986; Engwell et al. 2013; Cutler et al. 2016; Blong et al. 2017; Dugmore et al. 2018]. Thin deposits from successive small eruptions may be hard to distinguish and correlate in the geological record. Thus, quantification of the frequency of similar past events and the nature and extent of hazards at a volcano can be subject to large uncertainties. Rapid sampling and field quantification of tephra deposits in the aftermath of small eruptions is critical for gathering data on volcanic hazards.

El Salvador is one of the most exposed countries to natural hazards, and is subject to hurricanes, earthquakes, and volcanic eruptions [Rose et al. 2004]. It has the ninth highest level of volcanic threat globally, and over 2 million people live within 10 km of a volcano that has been active during the Holocene [Brown et al. 2015; Castro Carcamo and Gutiérrez 2021]. As of 2021, only 30 % of the Holocene-active volcanoes in El Salvador were monitored [Castro Carcamo and Gutiérrez 2021].

San Miguel volcano (known locally as Chaparrastique volcano), in south-eastern El Salvador (Figure 1), is the country's most active volcano and on 29th December 2013 it produced a VEI 2 explosive eruption [Escobar et al. 2016; Scarlato et al. 2016]. This 2130 mhigh composite volcano is located 12 km southwest of the town of San Miguel, the second largest urban area in the country. Over 60,000 people live within 10 km of

*Richard.brown3@durham.ac.uk
†retired
‡deceased

Editor: E. Liu/M. Heap | Typesetter: J. Farquharson

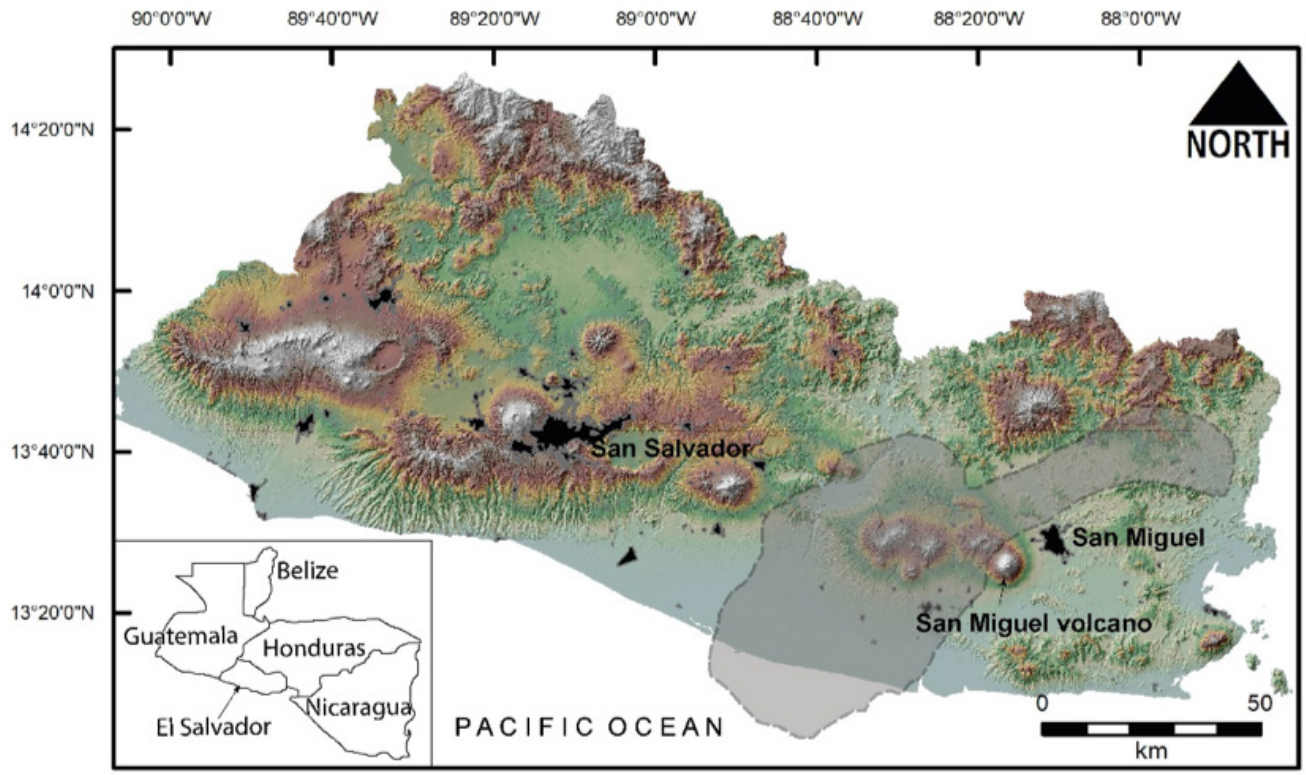

Figure 1: Digital elevation model of El Salvador showing location of San Miguel volcano, major urban areas (black), and extent of the 29th December ash cloud (grey) at approximately 18:45 CST on the 29th December 2013 (~5 hours after the end of the eruption). Ash cloud data modified from Jeff Schmaltz (LANCE/EOSDIS MODIS Rapid Response Team, GSFC).

the crater [GVP 2013]. Coffee plantations extend up to a few hundred metres from the summit on the eastern flanks.

Eruptions at the volcano pose a range of hazards to those who work on the flanks and to residents of towns close to the volcano [Major et al. 2001; Jiménez et al. 2018; 2019]. There are few scientific studies of the volcano and its past eruptions despite its frequent activity [Escobar 2003; Chesner et al. 2004]. Prior to the 2013 eruption, the volcano had experienced 40 years characterised only by small steam explosions, minor ash fall events, gas emissions, and rock falls, along with background-level seismic and degassing activity [Escobar 2003; Chesner et al. 2004; Pérez et al. 2006]. Since the 2013 eruption, the volcano has been in a state of unrest and has experienced elevated seismic and degassing activity, as well as minor ash eruptions and rock falls. Lahars have been generated on the flanks of the volcano. The 2013 eruption spurred interest in the volcano [Scarlato et al. 2016; Jiménez et al. 2018; 2019; 2020] and instigated international collaborations to improve the seismic, geodetic, and geochemical monitoring network around the volcano [Bonforte et al. 2016].

Here we examine, interpret, and quantify the 2013 eruption using video footage and photographs of the eruption sourced from the internet and taken by members of the public, and from government scientists who responded to the eruption. We integrate these data with an initial sedimentological and stratigraphic analysis of the pyroclastic deposits. This approach provides a wealth of information on this small-volume explosive eruption that could feed into hazard assessments at San Miguel, and other similar volcanoes, to better prepare authorities and populations for future eruptions. The study demonstrates the utility of crowd-sourced observations to help improve scientific understanding of volcanic eruptions [e.g. Wadsworth et al. 2022].

2 Background

2.1 San Miguel volcano

Volcanism in Central America is driven by the eastward subduction of the Cocos Plate beneath the Caribbean plate [Stoiber and Carr 1973; Carr et al. 2003]. The resultant Central American Volcanic Arc stretches along most of the west coast of Central America from Mexico to Costa Rica. El Salvador is home to numerous arc-related composite volcanoes, dacitic domes, monogenetic fields, and several silicic calderas, most of which sit in the Median Trough, a Plio-Pleistocene tectonic depression running parallel to the volcanic arc [Lexa et al. 2011].

San Miguel volcano is a large composite volcano with a symmetrical, concave-upwards morphology. The edifice is composed primarily of lava flows, with minor interbedded scoria and ash fall deposits. The summit crater is 900 m in diameter, 350 m deep, and has two partial flat benches at 2000 m a.s.l. (above sea level) on the eastern and western side of steep-sided a deeper inner crater, 500 m in diameter, with steep crater walls. The volcano has experienced two phases of growth: (1) initial cone growth from a central sum-

mit vent, and (2) flank eruptions and formation of the wide summit crater [Escobar 2003]. Eruptions have continued from both the summit crater and from flank vents located >5 km from the crater. Morphological and lithological evidence suggests that the volcano has experienced a debris avalanche–forming event in the past [Escobar 2003].

San Miguel volcano has erupted 28 times in the last 500 years, producing flank lava flows, and Strombolian ash-producing eruptions from the summit crater [Escobar 2003; Chesner et al. 2004]. Twelve lava-producing eruptions have occurred since 1699 CE [Chesner et al. 2004]. The latter have generated lava flows that reached 8 km from their vents. The crater formed by collapse during drainage of a shallow magma chamber by flank eruptions [Chesner et al. 2004]. Thirteen small-volume tephra producing eruptions have occurred since 1844 CE. Evidence in the geological record indicates at least one substantially larger tephra-producing eruption which may have occurred around 1500 CE [Escobar 2003; Chesner et al. 2004]. Block-and-ash flow deposits occur on the southwestern and eastern flanks of the volcano [Chesner et al. 2004]. Diffuse soil degassing levels are comparable to active volcanoes worldwide [Cartagena et al. 2004].

2.2 29th December 2013 eruption

San Miguel volcano erupted at 10:30 AM Central Standard Time (CST), on the 29th December 2013. From mid-November 2013, SO_2 output increased to above annual averages and doubled from ~330 t d^{-1} to 640 t d^{-1} between the 27th December and the eruption onset two days later [Granieri et al. 2015]. The eruption initiated with steam, gas, and weak ash emissions, prior to several powerful explosions that segued into a sustained eruption column that reached an altitude of 9.7 km a.s.l. [Escobar et al. 2016]. Workers in the coffee plantations reported falling ballistic blocks and several were hospitalised due to ash and gas exposure. There were no reported fatalities and the authorities evacuated ~3000 local residents from nearby towns.

Photographs and videos of the eruption indicate that atmospheric conditions during the eruption were clear: minimal cloud cover and cloud base at ~2 km a.s.l. Strong atmospheric wind shear meant that the eruption cloud was dispersed towards the west at altitudes of <6 km and towards the northeast at 9 km* (Figures 1 and 2).

The eruption ended around 12:45 PM CST on the same day, but elevated volcanic gas emissions continued for the next two days [Granieri et al. 2015]. Those authors report that SO_2 levels can reach hazardous levels above 900 m a.s.l. on the volcano.

Petrolological studies indicate that the eruption was triggered by the intrusion of hotter, basaltic magma into a shallow crustal reservoir of colder, basaltic andesite magma [Scarlato et al. 2016]. Textural and compositional characteristics of titanomagnetite and olivine, and inversely-zoned plagioclase are consistent with magma mixing [Scarlato et al. 2016]. Disequilibrium conditions in plagioclase rims resulted from crystallisation driven by decompression during rapid ascent to the surface (0.03 m s^{-1}) [Scarlato et al. 2016]. The juvenile material from the 2013 eruption is predominantly scoriaceous and basalt to basaltic andesite in composition (50–53 wt.% SiO_2) [Scarlato et al. 2016].

Weak ash-producing eruptions, gas emissions, and low-level seismicity have continued intermittently at the volcano since 2013 [GVP 2013]. Probabilistic eruption forecasting suggests that there is a low chance of a VEI >2 eruption occurring at San Miguel in the next ten years [Dzierma and Wehrmann 2014].

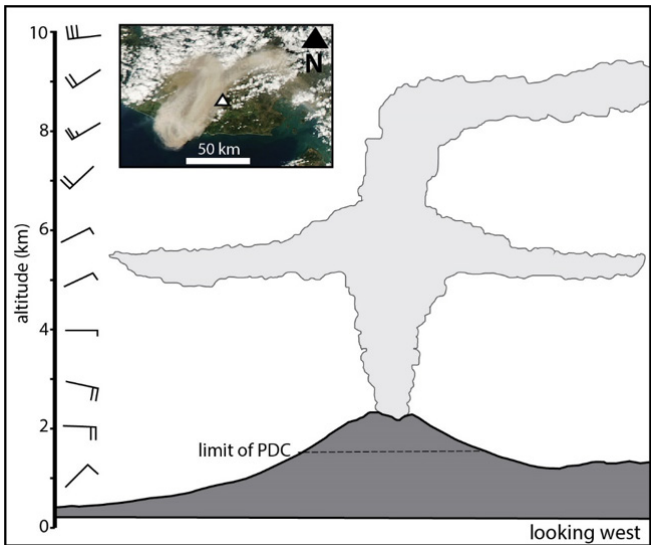

Figure 2: Schematic cross-section through the eruption column looking SW ~1 hour after eruption commenced. Eruption column structure has been reconstructed using photographs of eruption column. Wind barb vectors indicate strong wind shear at ~16 km a.s.l. (based on data from NASA/Washington VAAC: www.ssd.noaa.gov/VAAC/ARCH13/SANMIGU/2013L291751.html). Inset NASA Aqua MODIS image of ash cloud at 18:45 CST Image courtesy of Jeff Schmaltz LANCE/EOSDIS MODIS Rapid Response Team, GSFC (visibleearth.nasa.gov/images/82734/blast-from-san-miguel-volcano).

3 Methods

3.1 Photographs and video

The reconstruction of the 2013 eruption was accomplished via examination of photographs and videos of the eruption column from multiple sources. The primary data source was low-resolution time-lapse photography (1 frame per second) from a webcam operated by the *Ministerio del Ambiente y Recursos Naturales* (MARN), and situated on Pacaya volcano, 8 km NW of San Miguel volcano, that captured the entire duration of the eruption. All times given in this footage are approximate and based on the webcam frame counter.

In addition, we examined photographs and videos of the eruption taken by members of the public and sourced from the internet and social media. This video footage cumulatively exceeds an hour in length and is mostly focused on the first 15 minutes of the eruption. The location from where these photographs and videos were taken—and the time they were

*ssd.noaa.gov/VAAC/ARCH13/SANMIGU/2013L291751.html

taken—was not always clear, but has been estimated via clues such as the position of the sun, shadows, eruption phenomena, landmarks, and by comparison with the MARN video and satellite images on Google Earth taken in the months after the eruption. Hyperlinks to the videos, all hosted on YouTube.com at the time of publication, along with viewing direction, length, and key observations, are given in Table 1. Videos are referred to in the text by the number given in Table 1.

3.2 Fieldwork

We sampled the pyroclastic deposits over one week in early April 2014, still within the dry season and before rain had fallen, but the deposits, which were neither extensive nor thick, had been already widely removed by wind and by the post-eruption clean-up operation. We measured tephra fall thicknesses and collected tephra samples derived from fallout and a pyroclastic density current at 33 GPS points within the crater, on the flanks, and at distances of up to 30 km from the volcano. Strong summit degassing limited the time we could spend in the crater and the locations we could sample.

Ash fall deposits that we were confident had not been disturbed and that were representative of the original deposit were mostly confined to the crater and to flat surfaces such as tombstones, abandoned houses, and manhole covers. Ash fall deposits down to 1 mm in thickness were recognisable in these locations, but were commonly patchy. It proved difficult to sample thin ash fall layers without contamination from overlying or underlying ash layers. The orientations of tree trunks, felled by the pyroclastic density current on the upper flanks of the volcano, were measured using a compass clinometer.

3.3 Tephra characterisation

Tephra samples were sieved by hand (>3 ϕ) and analysed by laser diffraction using a Malvern Mastersizer at the University of Cambridge (<1 ϕ). The machine uses the Mie theory of light scattering. Results from the laser diffraction analysis were converted into weight percent (wt.%) using a constant clast density (2600 kg m^{-3}) and merged with the hand sieved results to produce complete grainsize distributions [Eychenne et al. 2012]. Grainsize distributions and statistics were analysed using the `GRADISTAT` software [Blott and Pye 2001]. Polymodal grainsize distributions were deconvolved into subpopulations with Weibull distributions using `DECOLOG 6.0` software* following Engwell and Eychenne [2016].

3.4 Tephra fall deposit volumes

The distribution of the tephra fall deposits and deposit volumes were calculated using both statistical and inversion modelling methods. The tephra fall deposits were reconstructed with thickness measurements at up to 33 locations west of the volcano. Isopachs were drawn by hand for the 20, 10, 5, and 2 mm deposit thicknesses. Areas were calculated using GIS software. Tephra volumes were calculated in `AshCalc` [Daggitt et al. 2014] using the exponential, power law, and Weibull methods.

Tephra fall distribution and deposit volume were also assessed using an inversion modelling approach with the probabilistic tephra dispersion model, `Tephra2` [Bonadonna 2006; Connor and Connor 2006]. `Tephra2` is a widely used [e.g. Fontijn et al. 2011; Johnston et al. 2012; Tsuji et al. 2017; Connor et al. 2019; Crummy et al. 2019] advection-diffusion model based on the work of Suzuki [1983] that describes diffusion, transport, and sedimentation of tephra particles released from an eruption column [Connor et al. 2001; Bonadonna 2005]. It calculates the total mass per unit area (kg m^{-2}) of tephra accumulation at individual grid locations by solving a simplified mass conservation equation. The mass conservation equation takes into account the distribution of tephra mass in the eruption column and particle settling velocity, as well as horizontal diffusion within the eruption column and atmosphere after the particle has been ejected from the plume [Connor et al. 2001; Bonadonna 2005; Connor and Connor 2006].

In order to solve the mass-conservation equation, `Tephra2` requires a number of input parameters to be defined. These include eruption source parameters such as vent location and height, grainsize distribution, particle density, eruption column height, and erupted mass. Where possible, eruption source parameters were derived from field observations and measurements (Table 2). Modelling parameters that describe the diffusion of particles in the plume and atmosphere, such as the eddy constant, diffusion coefficient, and fall time threshold, as well as the α and β parameters that describe the plume shape and wind data are also required (see Table 2 for details). We downloaded two years of NCEP/DOE Reanalysis II data provided by the NOAA Physical Sciences Laboratory, from 1st January 2013 to 31st December 2014, for 17 wind levels from approximately 100 to 30,000 m a.s.l., sampled 4 times daily (2920 files). Input parameters are adjusted in the `Tephra2` model using a non-linear inversion model to best match the measured tephra thickness and grain size distribution from the field data [Connor and Connor 2006]. The results were analysed and sorted according to the best fit, and those that were geologically inaccurate were discarded. Out of the remaining results, for consistency, the top 100 best fit were used to calculate the median. Tephra fallout thickness maps were generated by forward modelling the best-fit results.

3.5 Plume ejection velocities

Plume ejection velocities were estimated using images from a low-resolution time-lapse photography webcam operated by the *Ministerio del Ambiente y Recursos Naturales* (MARN). This webcam recording in the visible spectral range had a resolution of 640 × 480 pixels (px) at 1 frame per second (fps) and was located at 1270 m a.s.l. on the crater edge of El Pacayal volcano, 8 km NW of San Miguel volcano. Two methods of velocity extraction were applied, a manual and an automated approach. Manual velocity measurements were performed using the `MtrackJ` plug-in of the `ImageJ` software [Abràmoff et al. 2004]. It involves manually tracking the top part of individual vortexes over several frames (typically 2–10 frames). Due to the resolution of the camera as well as the distance

*https://www.lorenzo-borselli.eu/decolog/

Table 1: Web links to video footage of the 29th December 2013 eruption of San Miguel uploaded to YouTube as of November 2021. prefix = `https://www.youtube.com/watch?v=`. All video footage relates to Phase 1 of the eruption. PDC = pyroclastic density current; HD = high definition. Eruptive phases are described in Section 3.3.

#	Viewing direction	Duration (min:sec)	Eruptive phase	Web address	Comments
1	SW	2:28	1?	⟨prefix⟩ +CcveICyyD04	Best footage at 1:40; shows co-PDC cloud low on flanks.
2	N and SW	5:41	1	⟨prefix⟩ +tMcNBZE9sP0	2nd Vulcanian explosion, PDC and co-PDC cloud.
3	W	7:22	1	⟨prefix⟩ +jTKP8BwN6lY	Excellent footage of eruption column, and shearing by wind; co-PDC plumes rising from top of PDC on south and north side of volcano and merging with eruption column.
4	W	0:13		⟨prefix⟩ +9ZzTL_5Q_QQ	HD footage of rising eruption column.
5	N	6:25	1	⟨prefix⟩ +FwITy7gjX4g	PDC and eruption column.
6	N	6:42	1	⟨prefix⟩ +eeNFKRhSeuU	Rising eruption column; PDC and co-PDC plume.
7	various	4:06		⟨prefix⟩ +WnFDx57KQi0	Still footage spanning whole eruption; several unique views from west (e.g. 3:54 PDC on lower flanks).
8	S	7:17		⟨prefix⟩ +xKNGPFpPcD0	Video and stills; spanning whole eruption.
9	N	1:43		⟨prefix⟩ +KSBO0DiHEYw	Post-eruption helicopter flight over crater.
10	N?	10:00	?	⟨prefix⟩ +bbLaqnU0PM4	Zoomed-in footage of upper flanks and zone impacted by PDC.
11	SW	1:01		⟨prefix⟩ +mMmb0Xkz7y4	Eruption column and umbrella regions.
12	E	7:05		⟨prefix⟩ +NgLP-FzD32U	Eruption column and initial spread of umbrella region?
13	SE	4:29		⟨prefix⟩ +x5NOqUajIkk	Partial government webcam video (poor quality).
14	W	2:07		⟨prefix⟩ +6Kmzplb2SMw	Eruption column
15	W	0:29		⟨prefix⟩ +DJlgkXDUw-M	Good view of upper ash cloud extending to northeast taken from San Miguel city.
16	S	1:10	1	⟨prefix⟩ +1T9_UW4oTek	PDC and co-PDC cloud.
17	N?	1:07	1	⟨prefix⟩ +HfLyUYdrir4	Eruption column.
18	E/NE?	1:59	1	⟨prefix⟩ +penuSYAEP9Q	Under the umbrella cloud.
19	W	0:29		⟨prefix⟩ +Zu58f1XMh_s	Good footage of whole column and umbrella cloud spreading northeast.
20	S	1:43	1	⟨prefix⟩ +vECRJphlGNM	HD footage of PDC on western flank.
21	S	0:40		⟨prefix⟩ +awOE-YfICXI	Excellent view of entire eruption column.
22	E	0:55	1, 2	⟨prefix⟩ +KXOFxDTJnIY	Eruption column; umbrella regions; dilute cloud on lower western flanks.
23	SW	1:45	2	⟨prefix⟩ +drsnBpzr9Zk	Eruption column from San Miguel town.

to the volcanic plume, only large-scale vortices were tracked (hundreds of metres in diameter). To obtain velocities close to ejection velocities, velocity measurements were limited to heights of <500 m above the crater rim. This was the best compromise between the objective to perform measurements as close to the source as possible and the low resolution of the footage. The errors on velocity measurements are estimated to be $\pm 7\,\mathrm{m\,s^{-1}}$ on average.

The pixel size could not be calculated using optical equations; instead, we used a reference of known dimensions: the San Miguel crater diameter that we measured on both the footage and a DEM (approximately 760 m) in order to retrieve the pixel dimensions. The camera settings change during the video of the eruption and thus the pixel size was recalculated each time (see Supplementary Material 1). The second velocity extraction method consists in an automated approach using optical flow computer vision technique [Sun et al. 2010; 2014]. Following brightness constancy assumption over the measurement time, this method solves the optical flow equation based on pixel intensity [Baker et al. 2011]. An area of interest between 0 and 500 m above the crater rim was also set before running optical flow. Even though optical flow showed very

Table 2: Inversion modelling input parameters. British Geological Survey © UKRI 2022.

	Input			Source
	Parameter	Units	Value or range	
Vent	Vent easting*		362414	-
	Vent northing*		1485242	-
	Vent height†	m a.s.l.	1900	-
Eruption	Total erupted mass	kg	1×10^8–1×10^9	Statistical modelling
	Column height	m a.s.l.	4,000–6,000	Field observations
Grain size distribution	Grain size‡	ϕ	−6–7	Field data & model limitation
	Median phi‡	ϕ	1–6	Field data
	Standard deviation‡	ϕ	0.6–2	Field data
Tephra2 model	Eddy constant¶	$m^2\,s^{-1}$	0.04	-
	Diffusion coefficient§	$m^2\,s^{-1}$	200–2000	Inversion modelling
	Fall time threshold‖	s	100–10,000	Inversion modelling
	Lithic density#	$kg\,m^{-3}$	1900	Field data
	Pumice density#	$kg\,m^{-3}$	700	Field data
	Integration steps**		60	-
	Alpha α††		1–5	Inversion modelling
	Beta β††		0.01–5	Inversion modelling
Wind data	Speed‡‡	$m\,s^{-1}$	Randomly sampled	NCEP/DOE Reanalysis II
	Direction‡‡	°	Randomly sampled	NCEP/DOE Reanalysis II

* UTM;
† Metres above sea level;
‡ Tephra2 can only model the transport of particles over a range of grain size based on the settling velocity of particles in the atmosphere. Particles finer than 7ϕ will be dispersed far downwind and will have very different diffusion characteristics in the atmosphere [Connor and Connor 2006];
¶ Turbulence constant in the plume;
§ Diffusion coefficient for the horizontal diffusion of large particles: the larger the diffusion coefficient, the more widespread the plume;
‖ Threshold for change in diffusion law based on total particle fall time: allows fine particles to fall out;
Density varies linearly over particle range to approximate the change in density with particle size;
** The column is divided into horizontal layers, from the vent to the total eruption column height, each with its own uniform wind speed and direction;
†† The alpha and beta parameters describe the mass distribution of tephra within the plume: if α=β=1, then particles are dispersed uniformly; if α>β, then particles are concentrated in the top of the plume; if α<β, then particles are concentrated in the bottom of the plume;
‡‡ NCEP/DOE Reanalysis II wind data provided by the NOAA PSL, Boulder, Colorado, USA, from their website at https://psl.noaa.gov at the volcano location. Data vary with height, but are assumed to remain constant at each horizontal layer [Connor et al. 2001].

similar trends and absolute velocities to the manual approach, the results were quite noisy due to the poor resolution of the footage and we elected to focus on the manual approach. Reported velocities hereafter correspond to 2D vertical velocities not accounting for motion towards or away from the camera.

4 Results

4.1 Eruption chronology: evidence from video and photographs

Based on video analysis of plume type (gas, ash-rich, or ash-poor) and ascent speed, we divide the eruption into 5 phases (Figure 3). Here we describe the characteristics of each eruptive phase where the time in seconds given below relate to screen captures taken from the webcam (Figure 4).

4.1.1 *Phase 1 – Eruption commenced with Vulcanian explosions (approx.10:30–11:20 AM CST)*

Eruptive activity in the crater started with a water-rich plume that rose to heights of a few hundred metres above the crater. After approximately 7 minutes, an explosion propelled a dark, ash-laden eruption column into the air (63 s, Figure 4). Dust kicked up by the impact of ballistic blocks was visible on the western upper flanks of the volcano (118 s, Figure 4; video #5, Table 1). Less than a minute after the first explosion at least two more strong explosions occurred that expanded the column to the east and southwest. In photographs taken from

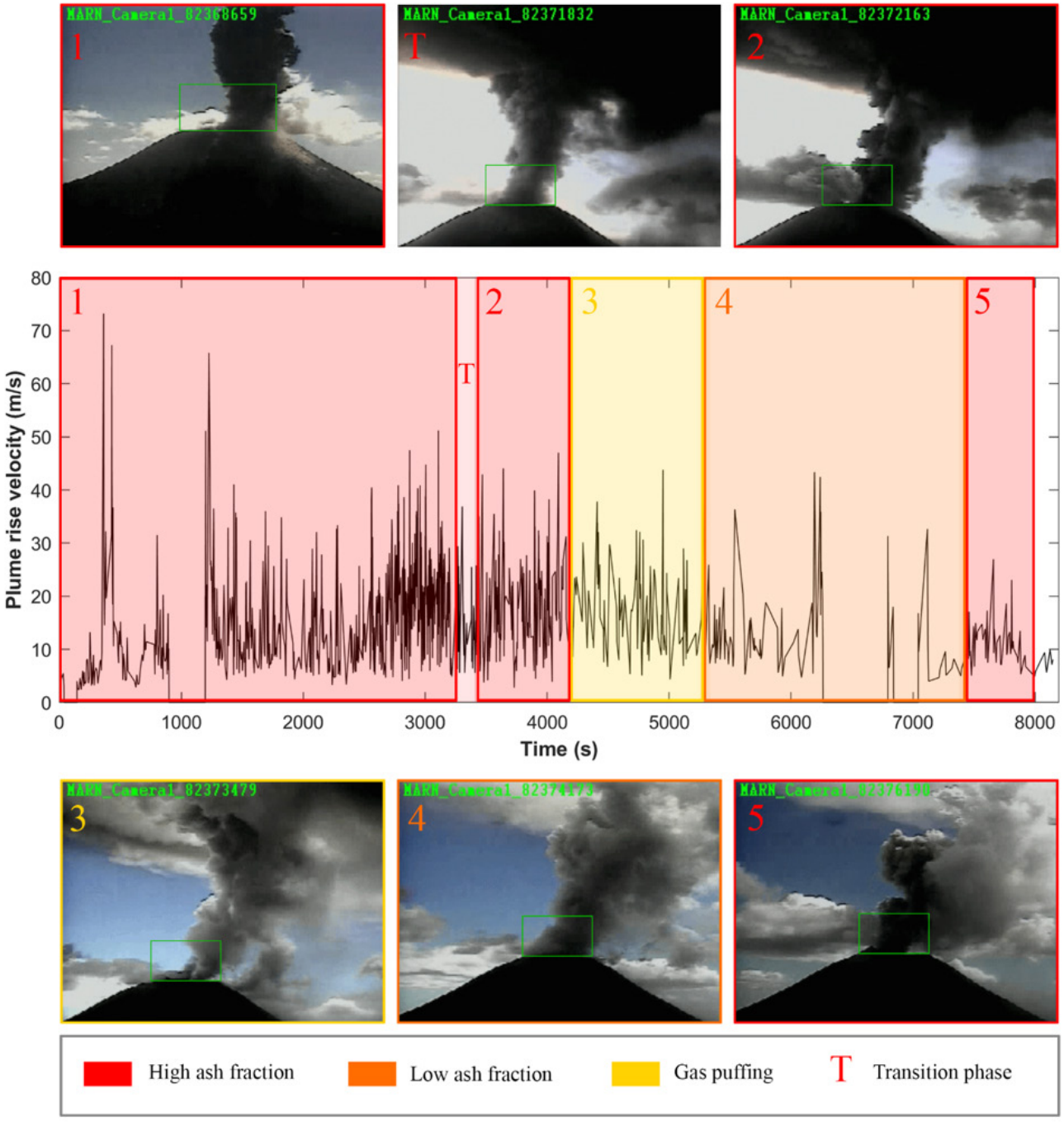

Figure 3: Eruptive phases derived from analysis of plume ascent speeds determined using time-lapse webcam images. Camera located at El Pacayal volcano, 8 km NW of San Miguel at 1270 m a.s.l. Numbers represented eruptive phases.

the south of the volcano, two distinct plumes are visible rising above the vent (video #5, Table 1). Estimated plume ascent speeds during the opening explosions exceeded 70 m s^{-1} (Figure 3).

Approximately ninety seconds after the first explosion, when the eruption column had reached a height of >1500 m above the crater, another vigorous explosion generated a column that rose immediately south of the earlier columns (151 s, Figure 4). Two columns are distinguishable in photographs taken from the southeast and have slightly different colours (Figure 5B, C, video #5, Table 1). The new eruption column rapidly rose to 400–500 m above the crater before parts of it collapsed to form a pyroclastic density current (PDC; video #5, Table 1). This PDC travelled radially out of the crater (186 s, Figure 4), and took 40–60 s to travel ~11 km down the upper flanks (slope angles of 23–26°). Based on this the estimated current velocities were 15–25 m s^{-1}. The PDC lofted and merged with the vent-derived eruption column.

Concurrently an ash cloud started advecting west at ~6 km a.s.l. (439 s, Figure 4). Parts of the eruption column

above the crater then expanded westwards, probably also advected by winds (551 s, Figure 4). Over the following 30 minutes, an ash cloud appeared to drift slowly down the western flank of the volcano at low altitude (218–1760 s, Figure 4). The initiation of this drifting ash cloud is unclear as the western side of the volcano is in shadow and the time-lapse video resolution is poor. Photographs and videos from other angles show ash filling the atmosphere between the ground and the spreading ash cloud at ~6 km altitude (videos #7, #16, #22, Table 1). A vigorously turbulent plume head was visible above the drifting ash cloud at ~4–5 km above sea level (864 s, Figure 4). One photo taken west of the volcano appears to show the southern margin of the drifting ash cloud on the ground (video #7, Table 1). As the ash cloud continued to drift west, it detached from the eruption column and separated from the overlying plume and umbrella cloud (see white arrow, 1760 s, Figure 4). This was advected westward by the prevailing winds. Tephra fell from the spreading umbrella cloud over the northwest flank of the volcano (e.g. 864 s, Figure 4). At approximately 11:25 AM CST, unwitting cumulus clouds, drifting from the east and level with the summit of the volcano, were entrained into the eruption column (Figure 5D and 5E).

For most of Phase 1, the eruption generated a sustained eruption column with maximum plume ascent speeds of 30–50 m s^{-1} (Figure 3). This plume rose to >9 km altitude and ash was advected west at ~6 km altitude and northeast at ~9 km altitude, due to strong wind shear (Figures 2 and 5). Phase 1 ended with a decrease in eruption intensity and a short period (8 minutes) without explosive activity (transition phase, Figure 3).

4.1.2 *Phase 2 (approx. 11:27 AM CST)*

The eruption restarted with closelytimed explosions that fed a sustained, dark, ash-rich eruption column with maximum plume ascent speeds of ~50 m s^{-1} (Figure 3). Videos taken from elsewhere around the volcano show that the ash cloud had started to advect northeast at 9 km altitude (videos #3, #4, #11, and #19, Table 1; Figure 5D).

4.1.3 *Phase 3 (approx. 11:43 AM CST)*

Phase 3 was characterised by a marked weakening of the eruption column. The time-lapse video shows the column gradually becoming paler in colour as the erupted ash content decreases. Maximum plume ascent speeds dropped below ~40 m s^{-1} and the plume head spread laterally into and just below the level of the umbrella cloud (Figure 3). The plume became markedly narrower towards the end of this phase and bent-over towards the west. Phase 3 ended with a vapour-rich, ash-poor (pale coloured) eruption column that detached from the suprajacent umbrella cloud, broke up and advected west at an altitude of 3.5–4 km.

4.1.4 *Phase 4 (approx. 12:00 PM CST)*

Phase 4 was marked by a brief (~5 minutes) increase in erupted ash content, inferred from the darker colour of the plume that fed a quasi-vertical eruption column. This transitioned into a weak, vapour-rich, ash-poor, inclined plume that rose to a height of several kilometres above the vent (Figure 3).

4.1.5 *Phase 5 (approx. 12:35 PM CST)*

This phase lasted 11 minutes and consisted of a series of closelytimed, ash-rich explosions that fed a weak, bent-over eruption column that rose to an altitude of 3.5–4 km before spreading. Plume ascent speeds were ~20 m s^{-1}. The column then detached from the vent and drifted westwards (Figure 3).

4.2 Pyroclastic deposits

4.2.1 *Pyroclastic density current deposits*

Satellite imagery indicates that the PDC generated in Phase 1 was dispersed across 3 km^2 of the upper flanks of the volcano (Figure 6). Videos from the helicopter flight over the volcano by MARN scientists on the 30th December clearly show the lobate margin of the area traversed by the PDC (videos #2, #9, Table 1). This was still visible on satellite imagery several months after the eruption (Figure 6). The PDC travelled farther down the north, west, and southwest flanks than the South and East flanks and lofted at an altitude of 1400–2000 m a.s.l.

Proximal pyroclastic density current deposits in the crater were sampled at two locations: on flat lava benches on the east and west sides of the crater (Figure 8). On the west bench the deposits reached several decimetres thick and MARN scientists reported up to 50 cm of tephra (fall deposits and pyroclastic density current deposits) around the crater the day after the eruption. The lowest layer consisted of several centimetres of moderately poorly sorted (characterised by an Inman [1952] sorting coefficient σ_ϕ of 2.5) tephra dominated by lithic clasts (64 wt.%). This was overlain by 15–45 cm of whitish-grey poorly sorted (σ_ϕ 2.3), ash-rich tephra with a normally-graded white ash top (σ_ϕ 3.0) [Figure 7; see also Escobar et al. 2016]. It was of similar composition to the underlying layer and contained 60 wt.% lithic clasts. Lapilli-sized clasts decrease in abundance upwards from 56–33 wt.%. On the eastern bench, the proximal PDC deposit consists of several decimetres of poorly sorted, diffusely bedded, lithic-rich tephra, that contains 28–45 wt.% lapilli-sized clasts (Figure 7). Proximal PDC deposits were very poorly sorted and have median diameters (Md_ϕ) of 0.5–1.5 (0.5–2 mm).

Distal PDC deposits were sampled on the upper north flank of the volcano where the PDC entered coffee plantations (Figure 7) at a distance of ~900 m from the vent. They consisted of lithic-rich, massive to weakly stratified ash with lapilli, were moderately sorted (σ_ϕ 1.54–1.6) and finer-grained (Md_ϕ 1–2) than proximal counterparts. Lapilli-sized clasts accounted for 2–20 wt.% of the deposits. The deposits had a maximum preserved thickness of 8 cm along gully floors, thinning to ~1 cm over ridges and were thicker on the upstream side of obstacles such as rocks or tree stumps. At locations where the deposits were thicker they consisted of a lower, coarser massive layer and an upper, finer-grained stratified layer.

The coffee plantations contain mature avocado trees that were damaged by the PDC over an area of ~0.22 km^2, at altitudes between 1500–1850 m (Figure 8). Trees with trunks up to 50 cm in diameter were uprooted (Figure 8B and 8C), snapped in half and, in some cases, transported several tens of metres downslope by the PDC. The trunks of fallen trees were aligned downslope. The PDC did not burn or delimb the trees

Figure 4: Time-lapse webcam images taken from El Pacayal volcano, 8 km NW of San Miguel, showing initial explosions, generation of the PDC and the drifting of the co-PDC cloud. View to the SE. Numbers in bottom left indicate time in seconds since first image. Camera moves and zooms several times during sequence. All photographs from Phase 1 of the eruption.

during uprooting or rupturing, and most fallen trees retained their crowns. The PDC deposit extended tens of metres into the plantation beyond the margin of tree damage, which was sharp (Figure 8C).

Estimating the volume of the PDC deposits is difficult due to lateral variations in thickness across topography. Additionally, limited time on the summit resulted in few sample locations and thickness measurements. Nevertheless, a volume can be approximated to a first order. The PDC was emplaced across an area of 3 km^2 over the upper flanks, and its deposit varies in thickness from 15–50 cm in the crater, and 1.5–10 cm on the flanks. Assuming the deposit was 30–50 cm thick everywhere in the crater (0.5 km^2), and 2–5 cm thick across the upper flanks, gives a deposit volume of ~2.7–3.7 × 10^5 m^3.

Rock surfaces around the summit and upper flanks, and trees within the damage zone, were plastered with a several-millimetre-thick, weakly lithified grey ash layer. This layer is visible on satellite images and photographs taken soon after the eruption (Figure 6, 7A, and 9A). The plastering of this layer onto vertical and overhanging rock faces indicates that it was wet and sticky on deposition and we attribute it to the PDC.

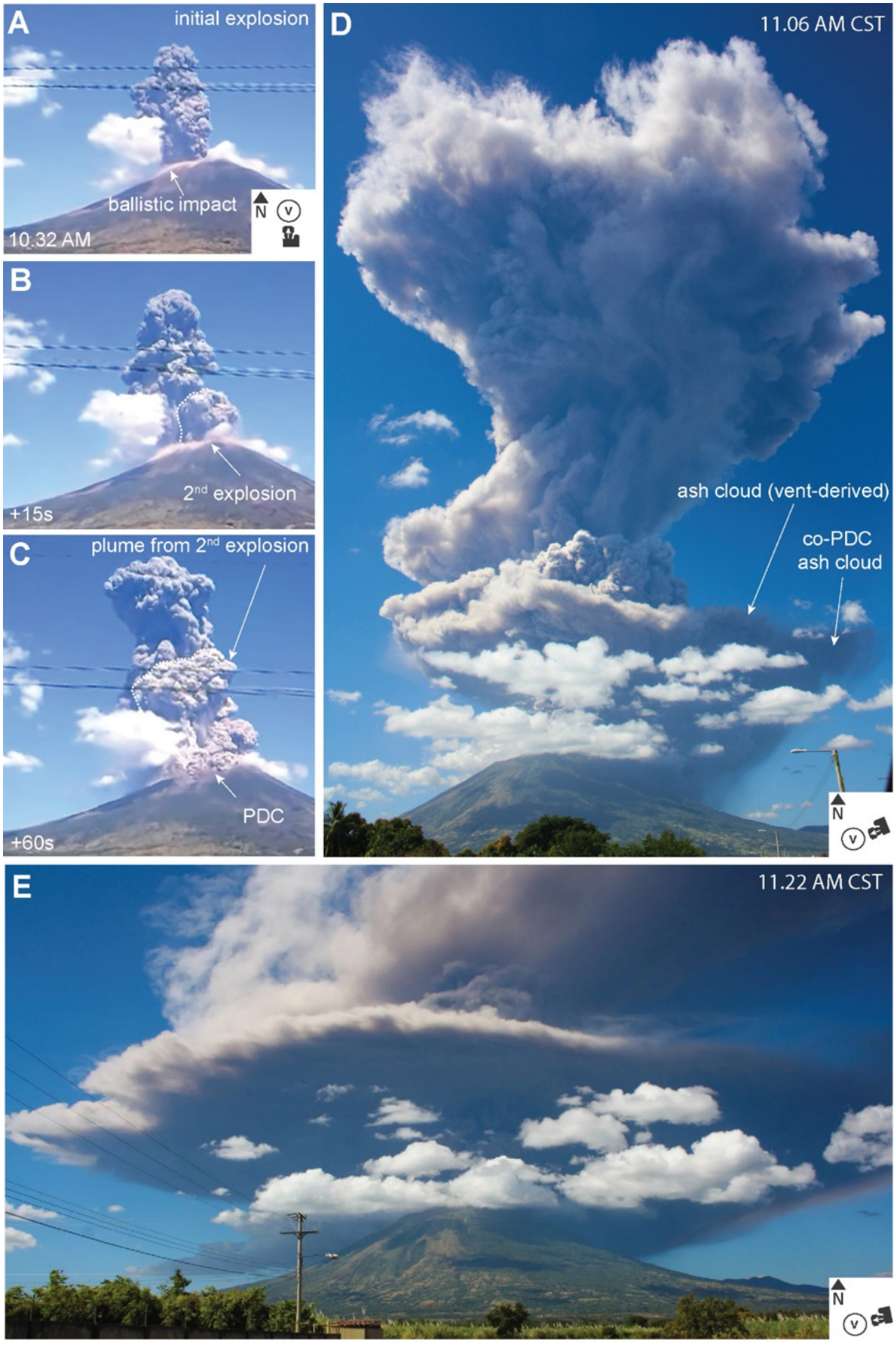

Figure 5: (Caption next page.)

Figure 5: (Previous page.) Photographs and video stills of the eruption column taken by observers on the ground. [A–C] Video stills (Video #5, Table 1) taken from the SW and showing the explosions prior to and responsible for the PDC. [D] Photo taken at 11:06 AM CST from 13°27'28.4"N 88°10'00.9"W (Calle Espana, San Miguel city) showing nascent ash cloud. Photo credit: Milton Parada. [E] Photo taken at 11:22 AM CST of the eruption column, showing the ash cloud at 5 km altitude. Photo taken from 13°25'52.1"N 88°10'30.1"W (South of San Miguel city). Camera symbols indicate approximate viewing direction. Photo credit: Milton Parada.

4.2.2 *Ballistic clasts*

Ballistic blocks up to 1.5 m in diameter, and mostly composed of variably altered lava, were ejected from the crater and scattered across the lava benches in the crater and over the upper flanks (Figure 9B–D). Juvenile bombs, up to 70 cm in diameter, occur within and around the crater. Some lithic blocks were enclosed by a layer of juvenile scoriaceous material. Ballistic clasts reached distances of 1.5 km from the vent and fell to altitudes as low as 1300 m a.s.l., on the flanks, well into coffee plantations where people were working. Some resulted in smouldering craters up to 1.4 m in diameter (Figure 9B). Post-impact rolling of ballistic blocks down the upper flanks was indicated by logjams of displaced ballistic blocks in gullies and ravines and by empty impact craters. Tongues of lithic blocks observed by MARN scientists at some locations on the upper flanks may have been deposited or moved by the PDC [Escobar et al. 2016].

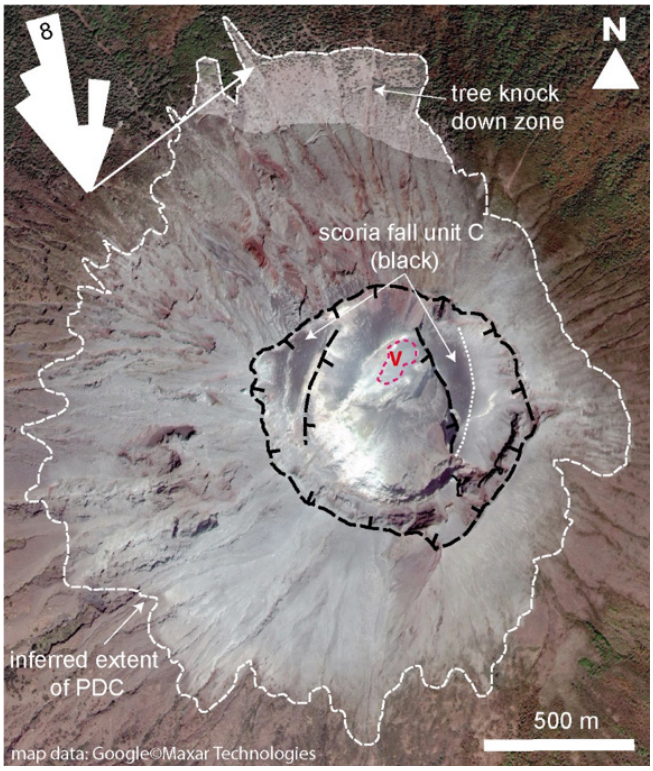

Figure 6: Google Earth satellite image from March 2014 showing inferred extent of the PDC (dashed white line), zone of knocked-down trees (shaded area) and crater (dotted black line). Unit C scoria fall deposit clearly visible on flat benches in crater (dark grey). Dotted white line shows extent of Unit C on eastern bench. Rose diagram shows orientation of trunks of fallen trees (n=30). v = inferred location of vent.

4.2.3 *Tephra fall deposits*

Tephra was deposited as far away as San Salvador (~100 km distance) and southern Honduras as the ash cloud dispersed. We observed three distinct tephra fall layers on the ground (units A, B, and C, Figure 10A), that we sampled at distances up to 36 km from the volcano. Beyond this, there was little ash preserved and it was heavily contaminated by dust, soil and vegetation. We infer that all tephra fall deposits accumulated during phase 1 of the eruption. We consider all the documented tephra fall deposits to belong to phases 1–2 of the eruption.

- Unit A

The lowermost unit was a pale grey, ash-aggregate-rich layer that varied from 40 mm thick on the upper flanks of the volcano to 1 mm thick at distances of 6 km (Figure 10A and 10B). Its dispersal axis has a bearing of N 80° W. The ash aggregates are structureless ash pellets and coated particles (AP1 and PC2 types of Brown et al. [2012]) that vary in diameter from <11 mm to >10 mm, and are weakly to moderately indurated. Where the deposit is >15 mm thick, the whole deposit is indurated. Towards the margins of the fall layer the deposit consists of scattered ash aggregates. The aggregated ash is composed predominantly of lithic particles.

- Unit B

Unit B is a grey, lithic-rich, fine-grained ash fall layer (Figure 10A and 10D) with a maximum observed thickness of 6 mm (3 km from crater) and was dispersed N 75° W. It was not identified at distances of <3 km from the crater. At distances exceeding 7 km from the vent, it is less than 1 mm thick and it became difficult to measure thickness accurately. It occurs in association with Unit C, even in distal locations 30 km from the crater (Figure 10D). In many places the contact between units B and C is hard to define.

- Unit C

The uppermost tephra fall layer is a lithic-poor (<9 wt.% lithic clasts) black scoria fall deposit (Figure 10A, 10C–D). It reaches 50 mm thick in the crater, and thins to <1 mm at distances of 30 km from the volcano. It was well preserved on the western crater bench and the margin of the fall deposit is visible on the eastern crater bench in satellite imagery (Figure 6) where it overlies the PDC deposit. Scattered scoria lapilli and juvenile bombs extend beyond the margin of the fall deposit. Unit C is less well preserved on the steep upper flanks of the volcano, potentially due to rolling of scoria clasts on landing or due to surface winds during and after the eruption.

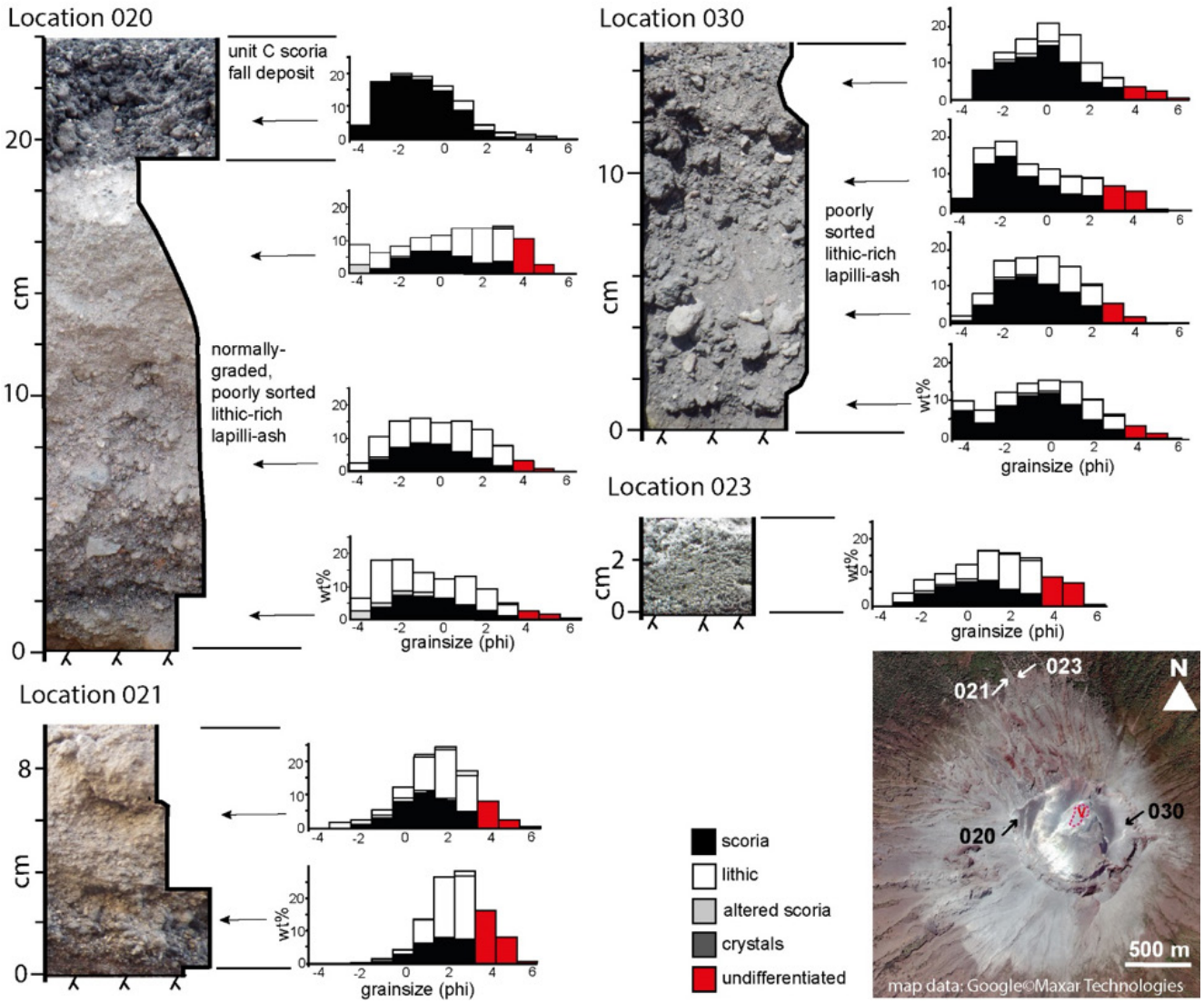

Figure 7: Sedimentary logs and grainsize histograms showing compositional data for the pyroclastic density current deposits. Inset image shows location of measured sections.

4.3 Pyroclast characteristics

Juvenile material ejected during the eruption was black scoria of basaltic to basaltic andesite composition (51–53 wt.% SiO_2 [Scarlato et al. 2016]). Juvenile clasts ranged in size from metre-sized bombs down to fine ash. A range of juvenile clast types were produced during the eruption: most are equant to oblate scoria with ragged exteriors, some of which had large, coalesced vesicles in the centre. A small proportion (<5 %) were distinctive plate scoria clasts [see Ruth and Calder 2014] with fused, wrinkled, and irregular exteriors. The phenocryst population was dominated by olivine and plagioclase with minor pyroxene and spinel: the groundmass is composed of matrix glass surrounding plagioclase, pyroxene, and spinel microlites (12 vol.%) [Scarlato et al. 2016].

Most scoria clasts contained inclusions of lithic clasts, either as ash-sized particles embedded in the groundmass, or as lapilli-sized clasts wrapped in scoria. Some of these lithic clasts were loose within their host scoria clasts. Cored juvenile bombs up to several decimetres in diameter occurred around the summit. Almost all juvenile clasts were partially covered in weakly indurated orange-brown lithic-rich volcanic ash, and 5–10 % of juvenile clasts in the Unit C fall deposit were partially to wholly covered in a mm-thick layer of pale grey ash, similar to the aggregates in the Unit A fall deposit. Where clasts are wholly covered in ash we classify them as coated particles [i.e. PC2 ash aggregates: Brown et al. 2012].

The lithic clast population was composed of variably hydrothermally altered lavas and scoria clasts, that varied in colour from white, to yellow, orange, red, and grey. Some clasts had amygdaloidal textures, and altered plagioclase, olivine, and pyroxene phenocrysts.

4.4 Grainsize characteristics of fall deposits

The thin nature of the ash fall layers meant that sampling of units B and C without contamination from the other was difficult and thus the grainsize distributions are variably bimodal and reflect mixing of the two layers. In order to extract mean-

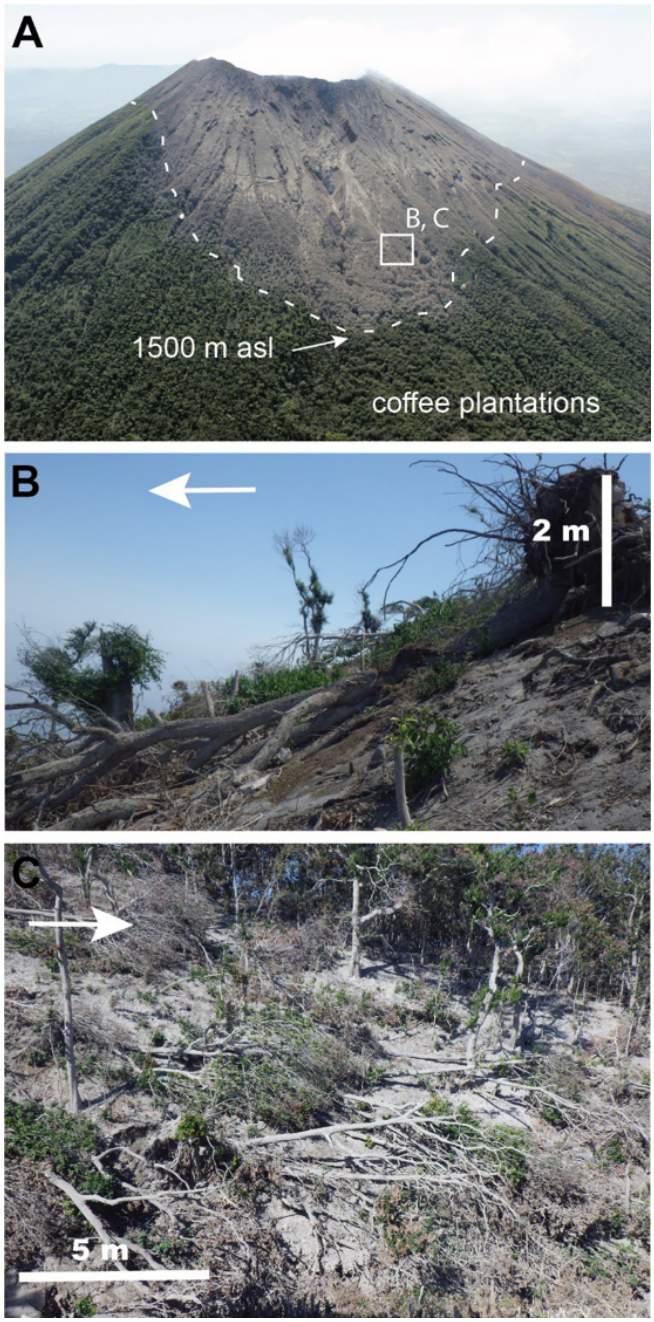

Figure 8: Vegetation damage from the pyroclastic density current on north flank of San Miguel. [A] View from helicopter from north showing the extent of the PDC (dashed line). White square shows approximate location of photographs [B] and [C]. Photo credit: Sandra Carranza. [B] Uprooted tree ~1 km from vent. Current travelled right to left. [C] Knocked-over trees with margin of devastated zone in background (standing trees). 1 km from crater. Current travelled left to right.

ingful grainsize data on the ash layers, we deconvolved the grainsize distributions using `DECOLOG 6.0` software*. This revealed that samples of both Unit B and Unit C are composed of: A) a coarse-grained subpopulation that decreases in size with distance from the volcano, and B) a fine-grained subpopulation that shows no clear decrease in median diameter with distance from vent (Figure 11B). We infer that the fine subpopulation represents Unit B while the coarse subpopulation represents Unit C. This is confirmed by visual observations of the ash fall layers (see Figure 10A and 10B).

*https://www.lorenzo-borselli.eu/decolog/

Table 3: Isopach thicknesses (T) and square root of areas ($\sqrt{A}$) for units A and B/C.

	$\sqrt{A}$ (km)	
T (mm)	Unit A	Unit B/C
20	0.88	0.84
10	1.46	1.76
5	2.43	2.73
2	4.86	6.95

4.5 Tephra dispersal and deposit volumes

The tephra fall deposits were dispersed westwards (~290°) from the volcano (Figure 12), consistent with predominant easterly winds at <6 km altitude (Figure 2). Isopach lines were constructed for 20, 10, 5, and 2 mm thicknesses: in more distal regions data were sparse and measured errors were large relative to deposit thickness (±50 %; Figure 12). Due to difficulties in separating unit B and C ash fall layers, we considered them together when calculating volumes. Calculated isopach areas are given in Table 3. Calculated tephra deposit volumes and input parameters using `AshCalc` [Daggitt et al. 2014] for units A and B/C are given in Table 4. The exponential model gives the lowest total tephra fall volume estimates (6×10^5 m^3) and the Weibull model the largest (1.05×10^6 m^3).

Inversion modelling of the combined B and C ash fall layers reveals a median eruption column height of 4041 m a.s.l., and a median erupted mass of 2.1×10^8 kg for the top 100 best-fit results. Assuming an average deposit density of 900 kg m^{-3}, this gives a median erupted volume of 2.33×10^5 m^3. The best fit parameters give an eruption column height of 5260 m a.s.l. and an erupted mass of 2.6×10^8 kg (Table 5), or 2.9×10^5 m^3. The resultant tephra dispersion map is presented in Figure 13.

5 Discussion

5.1 Eruptive parameters and sources of uncertainty

Plume velocity measurements have been performed based on a pixel size obtained using San Miguel's crater diameter as a reference. This method was applied due to unknown camera properties, tilt angle, and exact distance to the plume, and is a source of uncertainty. Velocity measurements performed here correspond to the observable external part of the plume where velocities are lower than at the centreline of the volcanic plume [Suwa et al. 2014; Suzuki et al. 2016]. The footage used has a frame rate of one frame per second thus providing a low temporal resolution of the plume motion. Finally, velocities have been extracted at altitudes up to 500 m above the crater rim, far away from the vent. For these reasons, the values

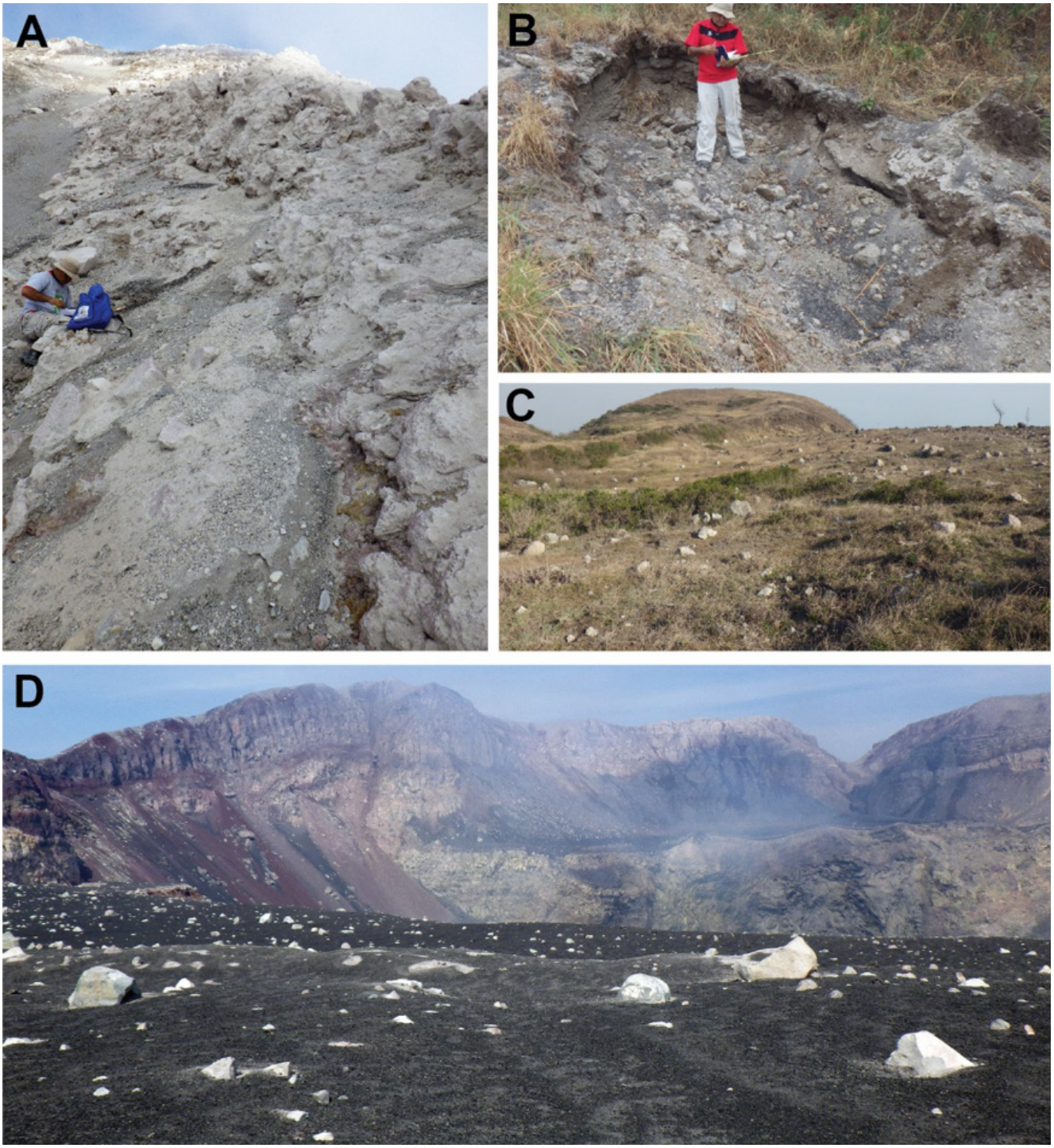

Figure 9: Proximal deposits of the 2013 eruption. [A] Indurated, grey ash coating on rocks on the western inner crater wall. [B] Large ballistic impact crater at 1360 m altitude on western flank, 1.6 km from the vent. [C] Ballistic clasts up to 70 cm in diameter littering upper SE flank. [D] View east over the western bench of the crater. Unit C scoria fall deposit and ballistic clasts in foreground. Crater in mid-ground. Eastern bench and crater wall in background. Ballistic clasts in foreground reach 70 cm in diameter.

provided here are conservative and represent a lower range of the velocity spectrum of the studied volcanic plume.

Measured absolute velocities fall in the range 10–70 m s^{-1}, in line with literature on short-lived Vulcanian plumes at Sakurajima, Colima, and Santiaguito volcanoes [Suwa et al. 2014; Webb et al. 2014; De Angelis et al. 2016; Tournigand et al. 2017]. However, the probable underestimation in our velocity results, together with the fact that San Miguel ejection phase lasted more than 2 h, point towards a sub-Plinian eruption category [Cioni et al. 2015]. This idea is confirmed by the velocity trend showing first a sudden intense release of energy with a clear peak in velocity followed by a steady state phase

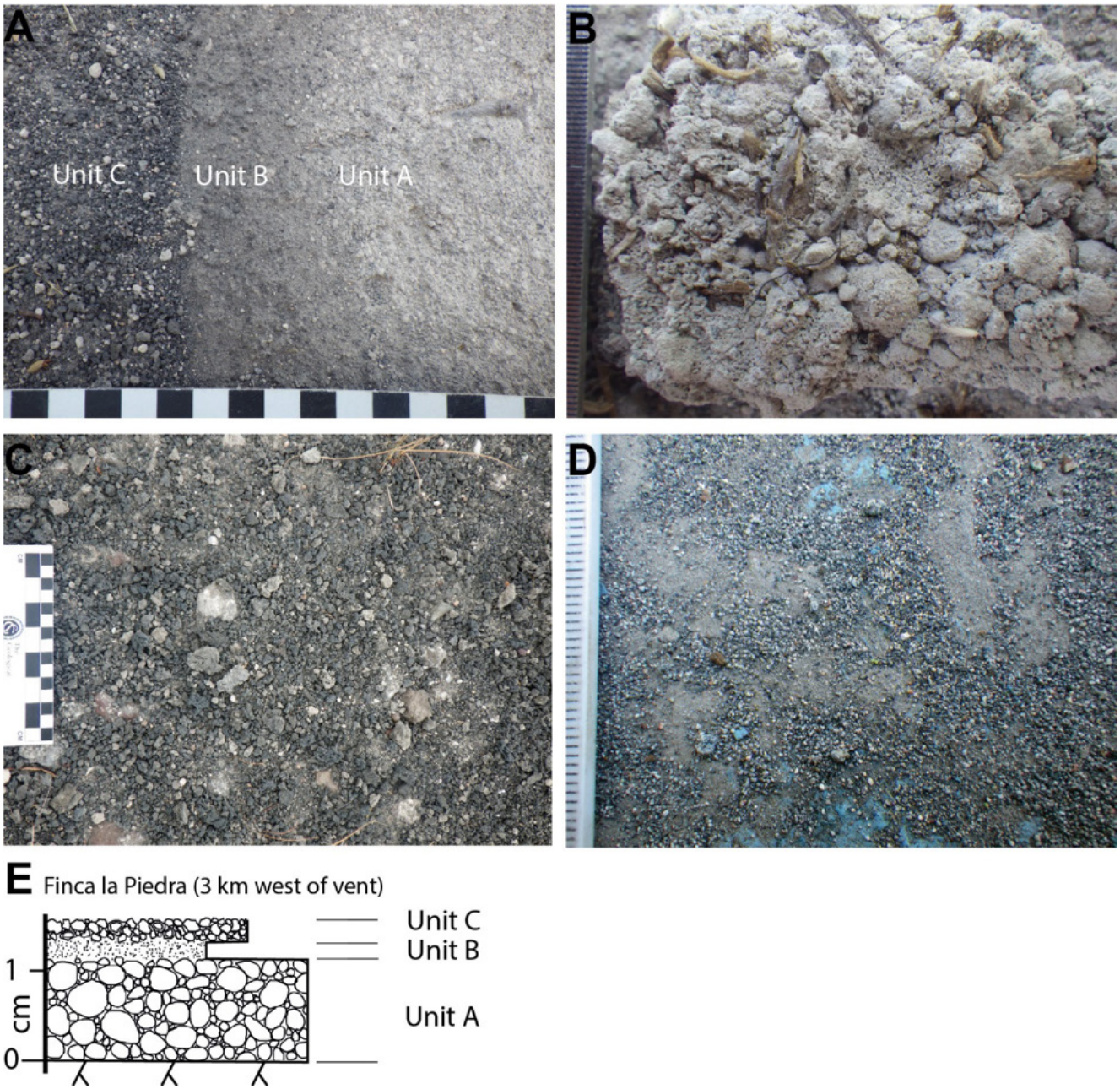

Figure 10: Fall deposits of the 2013 eruption of San Miguel volcano. [A] Units A, B, C, from right to left, 3 km west of the vent. Plan view of flat surface with layers partially swept. White clasts in Unit C are ash-coated scoria clasts. Scale is in centimetres. [B] Unit A at Finca La Piedra 2.7 km west of crater. Layer is composed of clast-supported ash aggregates of various sizes. Scale in half-millimetres. [C] Unit C 1.5 km west of crater. Smallest divisions on scale in centimetres. [D] Unit B and C at Chinameca cemetary, 13 km from the crater. Scale in millimetres. [E] Log through fall deposits at Finca la Piedra, 3 km west of the vent.

with a stable ejection (Figure 3). Furthermore, front velocity measurements during plume ascent do not show the transition between the gas-thrust and buoyancy phase because the camera field of view is too narrow (up to 1300 m above crater rim). The fact that such a transition did not happen within the first kilometre of plume ascent is consistent with a high-energy ejection compared to lower magnitude Vulcanian eruptions [Webb et al. 2014; Tournigand et al. 2017].

A first order estimate of the volume of tephra emitted by the 2013 eruption is ~10^6 m^3, giving a total erupted mass of ~9×10^8 kg, excluding the PDC deposit, and a DRE volume of 0.0003 km^3. We assume an average deposit density of 900 kg m^{-3}, and a DRE value of 2600 kg m^{-3} (calculated using whole rock data from Scarlato et al. [2016], and the `DensityX` program of Iacovino and Till [2019]). This makes the eruption VEI 2 (M = 1.9 [Pyle 2015]).

Uncertainties on these values stem from the lack of constraints on distal ash thickness and the limited number of thickness measurements, and we consider these conservative estimates. In many medial and distal locations, the ash fall

Table 4: Tephra volume estimates and input parameters for ash fall layers determined using `AshCalc` [Daggitt et al. 2014]. λ is the characteristic decay length scale of deposit thinning (in km) and k is a dimensionless shape parameter [see Bonadonna and Costa 2012].

Fall unit		volume (10^5 m^3)	segments	proximal limit	distal limit	λ	k
A	Exponential	1.99	2	0.1	10		
	Power law	2.35					
	Weibull	3.24				0.2–10	0–2.0
B/C	Exponential	4.18	2	0.1	30		
	Power law	6.01					
	Weibull	7.28				0.2–20	0–2.0

Table 5: `Tephra2` inversion best-fit parameters for the San Miguel 29th December 2013 eruption. British Geological Survey © UKRI 2022.

	Input			San Miguel eruption
	Parameter	Units	Value or range	
Eruption	Total erupted mass	kg	1×10^8–1×10^9	2.6×10^8
	Column height	m a.s.l.	4,000–6,000	5,260
Grain size distribution	Grain size	ϕ	−6–7	−6–7
	Median phi	ϕ	1–6	1
	Standard deviation	ϕ	0.6–2	2
`Tephra2` model	Eddy constant	m^2 s^{-1}	0.04	0.04
	Diffusion coefficient	m^2 s^{-1}	200–2000	299
	Fall time threshold	s	100–10,000	2,947
	Alpha α		1–5	1.5
	Beta β		0.01–5	4.4

layers were thin and it was difficult to separate units B and C during sampling, and therefore we have modelled tephra volumes of these deposits combined. Additionally, the dispersal of Unit B matches that of Unit C, even though its grainsize characteristics indicate that Unit B is probably derived from a co-PDC plume. The duration of the eruption responsible for tephra fall is estimated at ~4200 s, which spans phases 1 and 2 of the eruption (Figure 3). We calculate a time-averaged mass eruption rate of 2×10^5 kg s^{-1}, and a volumetric mass eruption rate of ~80 m^3 s^{-1}. This gives plume heights, calculated using the empirical relationships $H = 1.67Q^{0.259}$ [Sparks et al. 1997] and $H = 2.00Q^{0.241}$ [Mastin et al. 2009], of 5.2–5.7 km, in agreement with heights measured by radar, estimated from photographs, and derived from `Tephra2` models.

Uncertainties related to the inversion modelling result from many combinations of input parameters that can match the observed deposit thickness and grain size [Connor and Connor 2006; Scollo et al. 2008]. In order to account for this, `Tephra2` uses the downhill simplex algorithm [Nelder and Mead 1965; Connor and Connor 2006], a non-linear inversion model run in parallel on multiple processors, to search for the best-fit eruption parameter set that minimises the error between the measured tephra thickness and grain size distribution, and the model outputs [Connor and Connor 2006]. The non-linear inversion model systematically changes the parameters to find the optimal solution, or minima. Combinations of parameters define points in a dimensional space, and each point represents a vertex of a simplex. The algorithm shifts each vertex towards the centre of the simplex, where they converge at the optimal set of parameters [Connor and Connor 2006]. Simulations are run in parallel on multiple processors which allows rapid implementation of the physical model and a fully probabilistic analysis of tephra fall hazard [Bonadonna 2005]. Input parameters are often not well constrained; therefore stochastic sampling of parameter ranges is used allowing different scenarios to be investigated [Bonadonna 2005]. This approach means that more simulations are undertaken giving a better understanding of the full range of outcomes [Bonadonna 2005]. However, because there are multiple possible minima, there are uncertainties around whether the final output is the true best-fit [Johnston et al. 2012]. Running in parallel on multiple processors and stochastic sampling reduces this uncertainty;

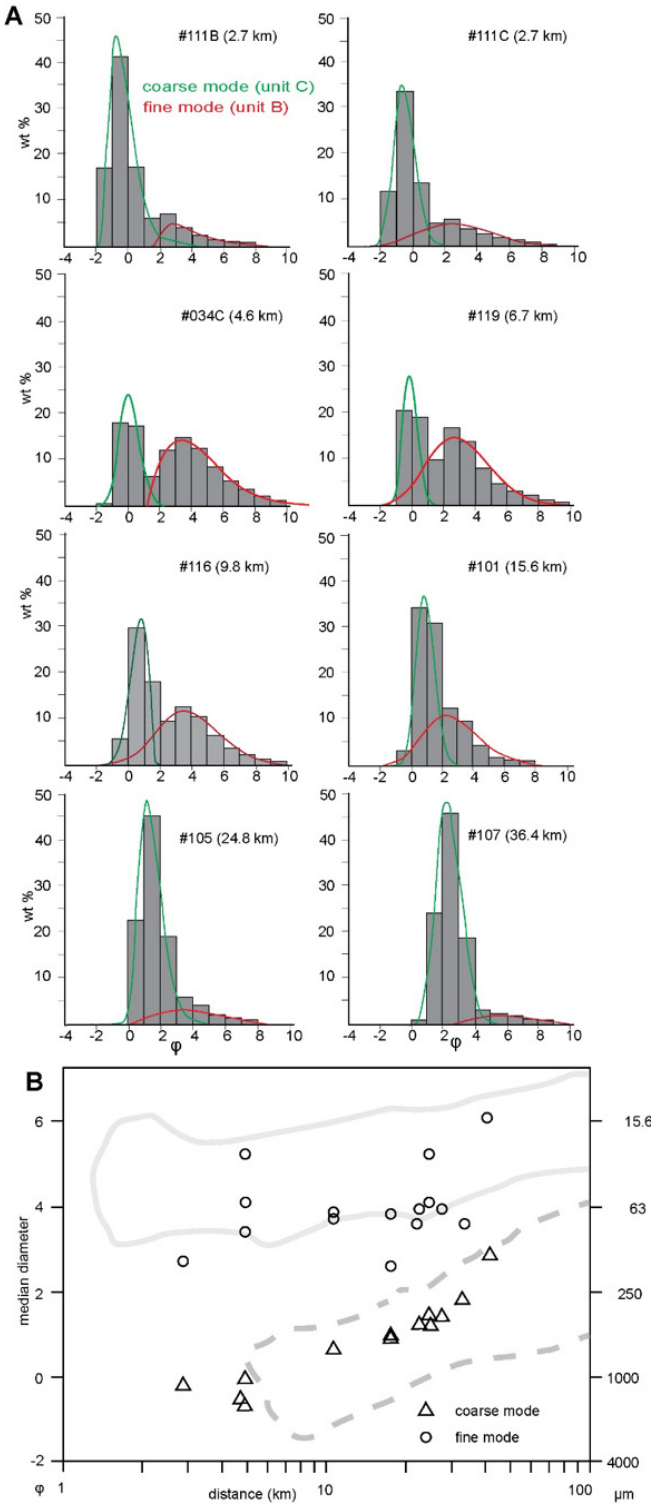

Figure 11: (Right.) Grainsize characteristics of tephra fall deposits. [A] Representative grainsize distributions at increasing distance from vent. Bimodal distributions represent cross contamination of units B and C during sampling. Grainsize distributions were deconvolved using DECOLOG 6.0 (https://www.lorenzo-borselli.eu/decolog/). [B] Median diameter vs distance derived from deconvolved coarse-grained and fine-grained grainsize subpopulations from samples of units B and C. Outlined fields are from Engwell and Eychenne [2016]: solid line is co-PDC deposits and fine peaks from bimodal fall deposits, dashed line is vent-sourced fall deposits and coarse peaks from bimodal fall deposits.

however results may still be false. To reduce this uncertainty further, we analysed the outputs and discarded any geologically inaccurate results. Scollo et al. [2008] provide more details on uncertainties related to tephra dispersion models.

5.2 Evolution of the eruption

The 2013 eruption of San Miguel was triggered when hot basaltic melt intruded into a shallow crustal magma reservoir containing colder basaltic andesite melt [Scarlato et al. 2016].

The eruption initiated with a series of vent-clearing explosions that propelled ash-laden columns into the air, and ejected large ballistics across the upper flanks of the volcano. The third major explosion produced a PDC that travelled 1 km down the flanks of the volcano, entered coffee plantations on the northern flank and knocked over trees before lofting (Figure 14). The collapse of the eruption column may have been caused by the inclusion of cold, dense lithic clasts and water into the eruption jet. The high lithic content and the lithology of the lithic clast population in the PDC deposit, predominantly hydrothermally altered lavas, are consistent with destruction of a shallow hydrothermal system. The presence of ash-aggregates, ash-coated scoria clasts and ash plastered to surfaces in the crater are consistent with the(se) explosion(s) being driven, in part, by phreatomagmatism involving rising

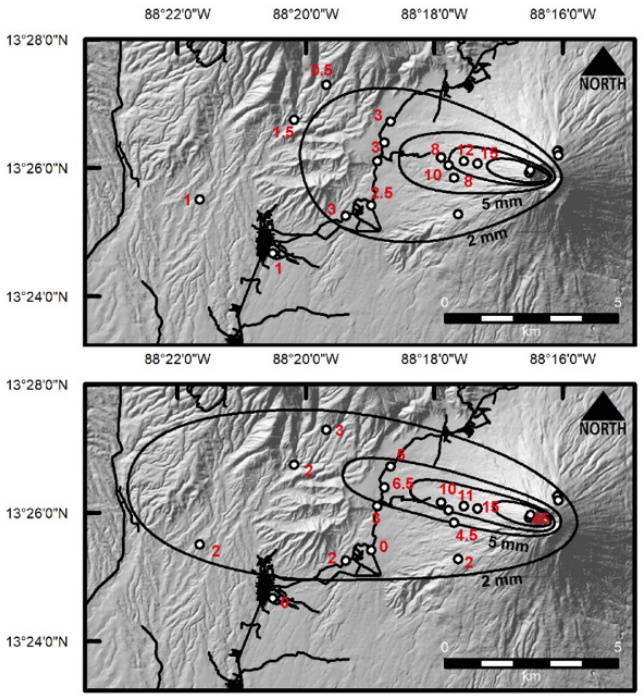

Figure 12: Isopach maps for tephra fall deposits of Unit A [top] and units B and C combined [bottom]. Isopachs drawn by hand. Contours are for 20, 10, 5, and 2 mm thickness. Red numbers indicate measured thickness of ash deposits on the ground.

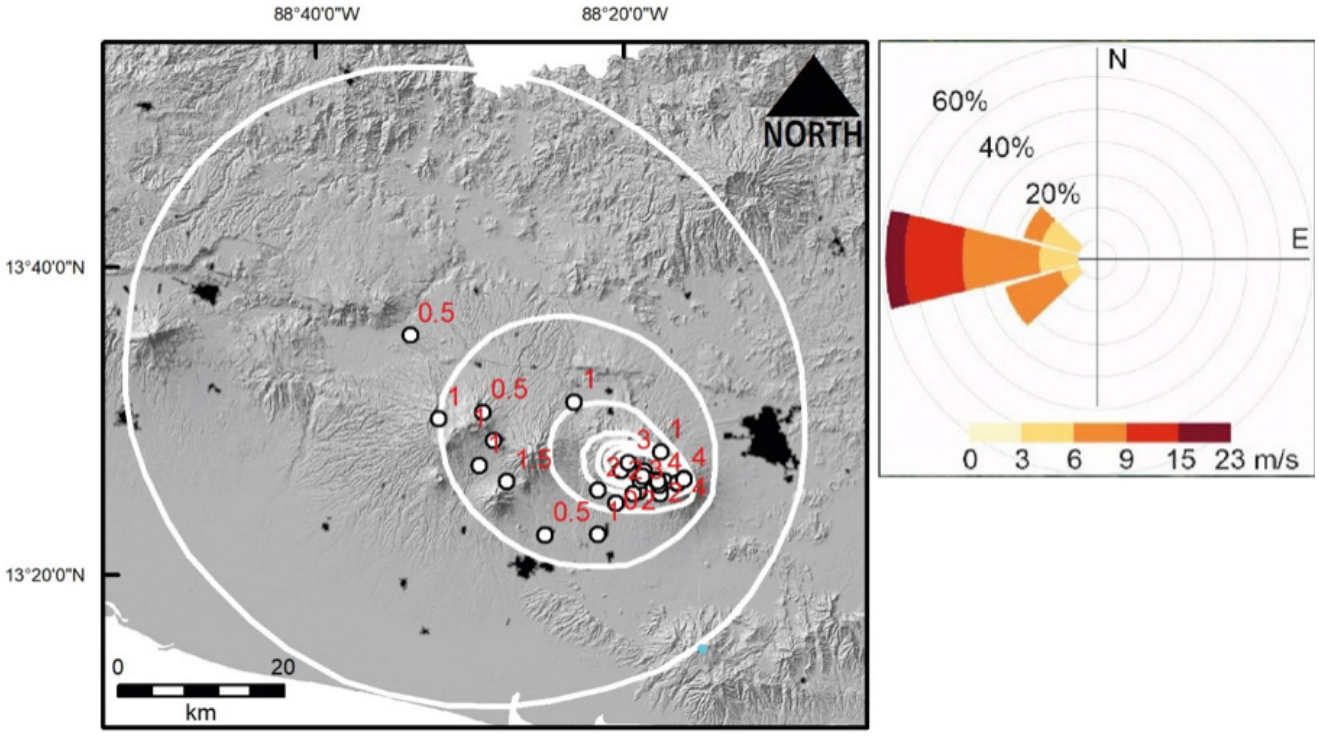

Figure 13: Tephra dispersion map output from `Tephra2`. Sample locations are shown as circles. Contours are of tephra fall thickness in millimetres: 1, 0.5, 0.25, 0.1, 0.05, 0.01, 0.001. Red numbers are the combined measured thicknesses of units B and C. The insets show the rose diagram for the best fit wind, with coloured bars showing the direction the wind is blowing. British Geological Survey © UKRI 2022.

magma and groundwater. The presence of juvenile material in the PDC deposit rules out a purely phreatic explosion. This interpretation is supported by evidence that the PDC did not char or incinerate vegetation upon entering coffee plantations, and was thus <250 °C [e.g. Scott 2000; Scott and Glasspool 2005]. The presence of low abundances of salt concentrations on the surfaces of ash particles within the ash aggregates supports explosive interaction with groundwater [Colombier et al. 2019].

The eruption then developed a quasi-steady, sub-Plinian convective column that ascended at 50–70 m s^{-1}. An umbrella cloud spread laterally at <6 km above sea level and advected westwards (Figure 14) and the column continued to ascent to ~9 km altitude and advected northeast (Figure 14). This gave the plume a crooked shape visible in a number of amateur videos (e.g. videos #4, #17, and #19, Table 1). The eruption column between the vent and the nascent ash cloud at <6 km altitude, expanded westwards (Figure 4, 439 s; Figure 14). Winds at this altitude blew from the east (Figure 2) and we infer that this material was ash lofted from the PDC (Figure 14). Video and photographic evidence (e.g. Figure 4) also document an ash cloud slowly drifting down the western flank (Figure 4, 864 s; Figure 14). There are no density current deposits on the lower western flanks of the volcano, and no damage to vegetation or buildings, suggesting that it was not in contact with the ground. Its dispersal matches that of Unit A ash aggregate-rich fall deposit, which would suggest that the ash cloud was cool and wet. This wet ash cloud may have been similar to fine-grained, ground-hugging phreatic eruption clouds documented at La Soufrière de Guadeloupe in 1976 [Heiken et al. 1980]. These ash clouds rose a few tensofmetres from the vent before moving downwind and down the flanks of the volcano and out to sea. They left behind thin ash layers containing ash aggregates. It is unclear if the wet ash cloud at San Miguel resulted from the PDC or from a separate phreatomagmatic explosion, but ash fall units A and B are not present in the crater, where instead Unit C overlies the PDC deposit. This suggests that the PDC and units A and B are related or coeval.

We infer that ash fall deposits units B and C fell from the westward-advected ash cloud during Phase 1 of the eruption (Figure 3). Deconvolution of the mixed grainsize distributions for samples of both units B and C reveal a fine-grained subpopulation that shows no clear decrease in median grainsize with distance (Unit B) and a coarse-grained subpopulation with a median grainsize that fines with distance from the vent (Unit C). The lack of clear fining with distance for Unit B, along with a median grainsize generally <63 µm (Figure 11B), is consistent with derivation from a co-PDC plume [Engwell and Eychenne 2016]. Additionally, there is no coarse-grained proximal tephra fall deposit correlating with Unit B. The fining trend of Unit C is consistent with deposition from an ash

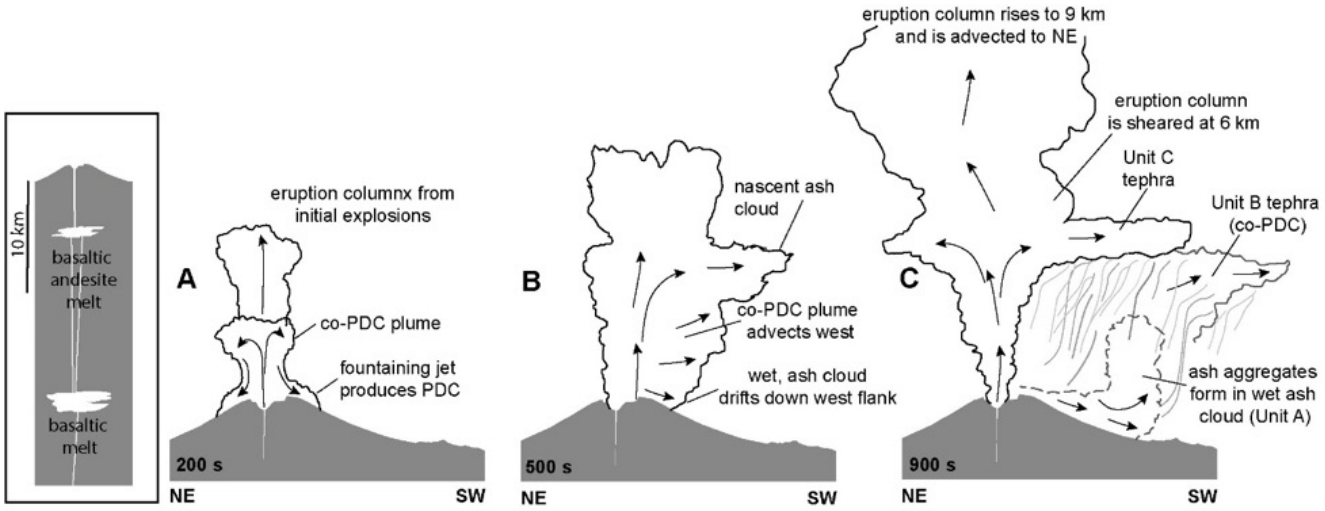

Figure 14: Schematic cartoons for the key stages during the opening 15 minutes of the eruption. Approximate timings given in seconds. Inset shows inferred magmatic plumbing system beneath San Miguel: eruption was triggered when hotter basaltic melt mixed with colder basaltic andesite melt in a shallow crustal magma reservoir [Scarlato et al. 2016].

cloud derived from a vent-fed eruption plume [e.g. Eychenne et al. 2012; 2015; Engwell and Eychenne 2016].

The main eruptive phases, phases 1 and 2 (Figure 3), lasted over an hour before transitioning into a phase of predominantly gas puffing (Phase 3, Figure 3), and weak, ash-poor explosions (Phase 4, Figure 3). Phase 5 was marked by several violent explosions that developed transient, bent-over eruption plumes that rose 2–3 km above the vent and were quickly dispersed by the wind (Figure 4). Some of these plumes developed weak and transient umbrella clouds. We did not recognise any fall deposits that we could relate to phases 3–5 around the volcano. We speculate that some of the ash-bearing plumes in phases 3–5 may have been generated by phreatic explosions or by rock falls and landslides within the crater.

5.3 Comparisons to past volcanic activity

Historic activity at San Miguel has included both explosive ash-producing eruptions from the summit crater and effusive flank eruptions [Escobar 2003; Chesner et al. 2004]. Prehistoric eruptions have produced PDCs as evidenced by block-and-ash flow deposits and by cross-stratified deposits, probably from phreatomagmatic explosions, preserved on the flanks of the volcano [Escobar 2003]. The largest known explosive eruption from the volcano had a DRE volume of 0.5 km^3, and emplaced a thick scoria fall deposit around the base of the volcano (the >1.8 ka Alpina Tephra [Escobar 2003]). Numerous thin tephra layers have been documented around San Miguel volcano and they indicate a long history of ash-producing explosive eruptions [Escobar 2003]. At least 18 of these have occurred since 1844 CE. Little is known about almost all historic explosive eruptions, as the eruptions were not documented and the deposits have been mostly eroded. The most recent explosive eruption, in 1970, dispersed about 7.5×10^4 m^3 of ash up to 10 km NE of the volcano [GVP 2013].

To the best of our knowledge, the 2013 eruption represents the largest explosive eruption from San Miguel in the past few hundred years and is the first historic eruption to generate a PDC. It is the only explosive eruption at the volcano where it has been possible to document the erupted products prior to erosion and removal by surface processes. Importantly it is the first eruption from the volcano captured extensively by video and photography, by both the government and by the public, from many different locations around the volcano. These data have been critical to understanding eruptive events, particularly in the first 20 minutes, and have revealed phenomena that would be hard to decipher solely from analysis of the deposits. It thus represents an exemplar case study to help model potential hazards from similar future explosive eruptions.

6 Conclusions

The 29th December 2013 VEI 2 eruption of San Miguel volcano, El Salvador, can be divided into 5 phases based on video analysis of the eruption column. Phases 1 and 2 (70 minutes total) were characterised by violent explosions and the establishment of a sub-Plinian eruption column that reached >9 km altitude. The end of Phase 1 was marked by a visible decrease in ash content in the eruption column and plume ascent speeds. Phase 3 (18 minutes) consisted of gas puffing. Phase 4 (35 minutes) comprised low ash content plumes with low ascent speeds. Phase 5 (11 minutes) recorded a brief uptick in activity with several vigorous transient explosions that produced weak ash-laden eruption columns that reached <2 km above the vent. We ascribe all of the pyroclastic deposits on the ground to Phase 1 of the eruption. Initial vent-clearing explosions were driven by explosive interaction between rising basaltic-andesite magma and groundwater that was probably hosted in a vent-housed hydrothermal system. These explosions showered ballistic blocks across the flanks of the volcano and generated a transient PDC that flowed into the coffee plantations on the upper flanks. In turn, the PDC generated a dilute, wet ash cloud that flowed at low velocities down the western flanks of the volcano and deposited a thin layer of ash

aggregates (Unit A ash fall deposit). At the same time, co-PDC ash advected westwards at ~5–6 km altitude and deposited the Unit B fall deposit. The Unit C scoria-rich fall deposit fell out from the westward-advected umbrella cloud at a similar altitude. The total deposit volume, including tephra fall and PDC deposits, is estimated at 10^6 m^3 (DRE 0.0003 km^3). The 2013 eruption was probably the largest historic explosive eruption from San Miguel volcano and provides a useful template for modelling future explosive eruptions. Crowd-sourced video footage and photographs of the eruption have proved critical in understanding the eruption processes, timings, and hazards. Authorities should seek to archive such resources for the 2013 eruption and for future eruptions in the country.

Author Contributions

RJB directed the research, sourced funding, undertook fieldwork, laboratory analysis, and wrote and edited the manuscript. WH, DE, EG undertook fieldwork and sampling. JC conducted the analysis in `Tephra2`. RPC conducted laboratory analysis of ash samples. P-YT conducted the video analysis of the eruption plume. All authors contributed to the editing and development of the manuscript.

Acknowledgements

This research was funded by a NERC Urgency Grant awarded to RJB (NE/M005003/1). Chris Rolfe at Cambridge University ran the laser diffraction grainsize analyses. We thank Milton Parada for sharing his photographs of the eruption. JC's contribution to this article was supported by British Geological Survey NC-ODA grant NE/R000069/1: Geoscience for Sustainable Futures, and publishes with permission of the Executive Director of the British Geological Survey (UKRI). PYT acknowledges the support of the Research Foundation Flanders (grant FWOTM996). We dedicate this paper to the memory of Eduardo Gutiérrez.

Data Availability

Grainsize data used in this paper is available here: https://doi.org/10.6084/m9.figshare.19952720.v1. Additional Supplementary Material is available alongside the online version of this article.

Copyright notice

References

Abràmoff, M. D., P. J. Magalhães, and S. J. Ram (2004). "Image processing with ImageJ". *Biophotonics international* 11(7), pages 36–42.

Baker, S., D. Scharstein, J. P. Lewis, S. Roth, M. J. Black, and R. Szeliski (2011). "A Database and Evaluation Methodology for Optical Flow". *International Journal of Computer Vision* 92(1), pages 1–31. DOI: 10.1007/s11263-010-0390-2.

Blong, R., N. Enright, and P. Grasso (2017). "Preservation of thin tephra". *Journal of Applied Volcanology* 6(1). DOI: 10.1186/s13617-017-0059-4.

Blott, S. J. and K. Pye (2001). "GRADISTAT: a grain size distribution and statistics package for the analysis of unconsolidated sediments". *Earth Surface Processes and Landforms* 26(11), pages 1237–1248. DOI: 10.1002/esp.261.

Bonadonna, C. (2005). "Probabilistic modeling of tephra dispersal: Hazard assessment of a multiphase rhyolitic eruption at Tarawera, New Zealand". *Journal of Geophysical Research* 110(B3). DOI: 10.1029/2003jb002896.

– (2006). "Probabilistic modelling of tephra dispersion". In: *Statistics in Volcanology*. Edited by H. M. Mader, S. G. Coles, C. B. Connor, and L. J. Connor. The Geological Society of London on behalf of The International Association of Volcanology and Chemistry of the Earth's Interior, pages 243–259. DOI: 10.1144/iavcei001.19.

Bonadonna, C. and A. Costa (2012). "Estimating the volume of tephra deposits: A new simple strategy". *Geology* 40(5), pages 415–418. DOI: 10.1130/g32769.1.

Bonforte, A., D. A. Hernandez, E. Gutiérrez, L. Handal, C. Polío, S. Rapisarda, and P. Scarlato (2016). "The unrest of the San Miguel volcano (El Salvador, Central America): installation of the monitoring network and observed volcano-tectonic ground deformation". *Natural Hazards and Earth System Sciences* 16(8), pages 1755–1769. DOI: 10.5194/nhess-16-1755-2016.

Brown, R. J., C. Bonadonna, and A. J. Durant (2012). "A review of volcanic ash aggregation". *Physics and Chemistry of the Earth, Parts A/B/C* 45–46, pages 65–78. DOI: 10.1016/j.pce.2011.11.001.

Brown, S. K., M. R. Auker, and R. S. J. Sparks (2015). "Populations around Holocene volcanoes and development of a Population Exposure Index". In: *Global Volcanic Hazards and Risk*. Cambridge University Press, pages 223–232. DOI: 10.1017/cbo9781316276273.006.

Carr, M. J., M. D. Feigenson, L. C. Patino, and J. A. Walker (2003). "Volcanism and geochemistry in Central America: Progress and problems". *Geophysical Monograph-American Geophysical Union* 138, pages 153–174. DOI: 10.1029/138GM09.

Cartagena, R., R. Olmos, D. L. López, T. Soriano, F. Barahona, P. A. Hernández, and N. M. Pérez (2004). "Diffuse soil degassing of carbon dioxide, radon, and mercury at San Miguel volcano, El Salvador". In: *Natural Hazards in El Salvador*. Edited by W. I. Rose, J. J. Bommer, D. L. López, M. J. Carr, and J. J. Major. Geological Society of America. DOI: 10.1130/0-8137-2375-2.203.

Castro Carcamo, R. A. and E. Gutiérrez (2021). "Volcanic monitoring and hazard assessment in El Salvador". *Volcanica* 4(S1), pages 183–201. DOI: 10.30909/vol.04.s1.183201.

Chesner, C. A., C. R. Pullinger, and C. D. Escobar (2004). "Physical and chemical evolution of San Miguel volcano, El Salvador". In: *Natural Hazards in El Salvador*. Edited by W. I. Rose, J. J. Bommer, D. L. López, M. J. Carr, and J. J. Major. Geological Society of America. DOI: 10.1130/0-8137-2375-2.213.

Cioni, R., M. Pistolesi, and M. Rosi (2015). "Plinian and Subplinian Eruptions". In: *The Encyclopedia of Volcanoes*. Edited by H. Sigurdsson. Elsevier, pages 519–535. DOI: 10.1016/b978-0-12-385938-9.00029-8.

Collins, B. D., T. Dunne, and A. K. Lehre (1983). "Erosion of tephra-covered hillslopes north of Mount St. Helens, Washington: May 1980–May 1981". *Zeitschrift für Geomorphologische Naturwissenschaftliche Forschung* 16(1), pages 103–121.

Collins, B. D. and T. Dunne (1986). "Erosion of tephra from the 1980 eruption of Mount St. Helens". *Geological Society of America Bulletin* 97(7), page 896. DOI: 10.1130/0016-7606(1986)97<896:eotfte>2.0.co;2.

Colombier, M., S. B. Mueller, U. Kueppers, B. Scheu, P. Delmelle, C. Cimarelli, S. J. Cronin, R. J. Brown, M. Tost, and D. B. Dingwell (2019). "Diversity of soluble salt concentrations on volcanic ash aggregates from a variety of eruption types and deposits". *Bulletin of Volcanology* 81(7). DOI: 10.1007/s00445-019-1302-0.

Connor, C. B., L. J. Connor, C. Bonadonna, J. Luhr, I. Savov, and C. Navarro-Ochoa (2019). "Modelling tephra thickness and particle size distribution of the 1913 eruption of Volcán de Colima, Mexico". In: *Volcán de Colima: Portrait of a Persistently Hazardous Volcano*. Edited by N. Varley, C. B. Connor, and J.-C. Komorowski. Springer, pages 81–110. DOI: 10.1007/978-3-642-25911-1_3.

Connor, C. B., B. E. Hill, B. Winfrey, N. M. Franklin, and P. C. La Femina (2001). "Estimation of Volcanic Hazards from Tephra Fallout". *Natural Hazards Review* 2(1), pages 33–42. DOI: 10.1061/(asce)1527-6988(2001)2:1(33).

Connor, L. J. and C. B. Connor (2006). "Inversion is the key to dispersion: understanding eruption dynamics by inverting tephra fallout". *Statistics in Volcanology*, pages 231–242. DOI: 10.1144/iavcei001.18.

Crummy, J. M., I. P. Savov, S. C. Loughlin, C. B. Connor, L. Connor, and C. Navarro-Ochoa (2019). "Challenges of determining frequency and magnitudes of explosive eruptions even with an unprecedented stratigraphy". *Journal of Applied Volcanology* 8(1), pages 1–14. DOI: 10.1186/s13617-019-0083-7.

Cutler, N. A., R. M. Bailey, K. T. Hickson, R. T. Streeter, and A. J. Dugmore (2016). "Vegetation structure influences the retention of airfall tephra in a sub-Arctic landscape". *Progress in Physical Geography: Earth and Environment* 40(5), pages 661–675. DOI: 10.1177/0309133316650618.

Daggitt, M. L., T. A. Mather, D. M. Pyle, and S. Page (2014). "AshCalc–a new tool for the comparison of the exponential, power-law and Weibull models of tephra deposition". *Journal of Applied Volcanology* 3(1). DOI: 10.1186/2191-5040-3-7.

De Angelis, S., O. D. Lamb, A. Lamur, A. J. Hornby, F. W. von Aulock, G. Chigna, Y. Lavallée, and A. Rietbrock (2016). "Characterization of moderate ash-and-gas explosions at Santiaguito volcano, Guatemala, from infrasound waveform inversion and thermal infrared measurements". *Geophysical Research Letters* 43(12), pages 6220–6227. DOI: 10.1002/2016gl069098.

Dugmore, A., R. Streeter, and N. Cutler (2018). "The role of vegetation cover and slope angle in tephra layer preservation and implications for Quaternary tephrostratigraphy". *Palaeogeography, Palaeoclimatology, Palaeoecology* 489, pages 105–116. DOI: 10.1016/j.palaeo.2017.10.002.

Dzierma, Y. and H. Wehrmann (2014). "Probabilities of future VEI ≥ 2 eruptions at the Central American Volcanic Arc: a statistical perspective based on the past centuries' eruption record". *International Journal of Earth Sciences* 103(7), pages 2029–2042. DOI: 10.1007/s00531-012-0803-2.

Engwell, S. L. and J. Eychenne (2016). "Contribution of Fine Ash to the Atmosphere From Plumes Associated With Pyroclastic Density Currents". In: *Volcanic Ash*. Edited by S. Mackie, K. Cashman, H. Ricketts, A. Rust, and M. Watson. Elsevier, pages 67–85. DOI: 10.1016/b978-0-08-100405-0.00007-0.

Engwell, S. L., R. S. J. Sparks, and W. P. Aspinall (2013). "Quantifying uncertainties in the measurement of tephra fall thickness". *Journal of Applied Volcanology* 2(1). DOI: 10.1186/2191-5040-2-5.

Escobar, C. D. (2003). "San Miguel volcano and its volcanic hazards, El Salvador". PhD thesis. Michigan Technological University.

Escobar, C. D., E. Gutiérrez, and F. Montalvo (2016). "Actividad del volcán Chaparrastique durante los años 2013 y 2014 Ministerio de Medio Ambiente y Recursos Naturales Abril, 2016". *Report of the Ministerio de Medio Ambiente y Recursos Naturales*, pages 1–39.

Eychenne, J., K. Cashman, A. Rust, and A. Durant (2015). "Impact of the lateral blast on the spatial pattern and grain size characteristics of the 18 May 1980 Mount St. Helens fallout deposit". *Journal of Geophysical Research: Solid Earth* 120(9), pages 6018–6038. DOI: 10.1002/2015jb012116.

Eychenne, J., J.-L. Le Pennec, L. Troncoso, M. Gouhier, and J.-M. Nedelec (2012). "Causes and consequences of bimodal grain-size distribution of tephra fall deposited during the August 2006 Tungurahua eruption (Ecuador)". *Bulletin of Volcanology* 74(1), pages 187–205. DOI: 10.1007/s00445-011-0517-5.

Fontijn, K., G. G. J. Ernst, C. Bonadonna, M. A. Elburg, E. Mbede, and P. Jacobs (2011). "The ~4-ka Rungwe Pumice (South-Western Tanzania): a wind-still Plinian eruption". *Bulletin of Volcanology* 73(9), pages 1353–1368. DOI: 10.1007/s00445-011-0486-8.

Global Volcanism Program (GVP) (2013). "San Miguel (343100)". In: *Volcanoes of the World, v. 4.11.0*. Edited by E. Venzke. Smithsonian Institution. DOI: 10.5479/si.GVP.VOTW4-2013.

Granieri, D., G. Salerno, M. Liuzzo, A. La Spina, G. Giuffrida, T. Caltabiano, G. Giudice, E. Gutierrez, F. Montalvo, M. R. Burton, and P. Papale (2015). "Emission of gas and atmospheric dispersion of SO2during the December 2013 eruption at San Miguel volcano (El Salvador, Central America)". *Geophysical Research Letters* 42(14), pages 5847–5854. DOI: 10.1002/2015gl064660.

Heiken, G., B. Crowe, T. McGetchin, F. West, J. Eichelberger, D. Bartram, R. Peterson, and K. Wohletz (1980). "Phreatic eruption clouds: the activity of la Soufrière de Guadeloupe, F.W.I., August — October, 1976". *Bulletin Volcanologique* 43(2), pages 383–395. DOI: 10.1007/bf02598039.

Iacovino, K. and C. B. Till (2019). "DensityX: A program for calculating the densities of magmatic liquids up to 1,627 C and 30 kbar". *Volcanica* 2(1), pages 1–10. DOI: 10.30909/vol.02.01.0110.

Inman, D. L. (1952). "Measures for Describing the Size Distribution of Sediments". *SEPM Journal of Sedimentary Research* 22(3), pages 125–145. DOI: 10.1306/d42694db-2b26-11d7-8648000102c1865d.

Jiménez, D., L. Becerril, S. Bartolini, C. D. Escobar, and J. Martí (2020). "Making a qualitative volcanic-hazards map by combining simulated scenarios: An example for San Miguel Volcano (El Salvador)". *Journal of Volcanology and Geothermal Research* 395, page 106837. DOI: 10.1016/j.jvolgeores.2020.106837.

Jiménez, D., L. Becerril, S. Bartolini, and J. Martí (2018). "Spatio-temporal hazard estimation in San Miguel volcano, El Salvador". *Journal of Volcanology and Geothermal Research* 358, pages 171–183. DOI: 10.1016/j.jvolgeores.2018.04.003.

Jiménez, D., L. Becerril, A. Carballo, S. Baires, and J. Martí (2019). "Estimating exposure around San Miguel Volcano, El Salvador". *Journal of Volcanology and Geothermal Research* 386, page 106675. DOI: 10.1016/j.jvolgeores.2019.106675.

Johnston, E. N., J. Phillips, C. Bonadonna, and I. Watson (2012). "Reconstructing the tephra dispersal pattern from the Bronze Age eruption of Santorini using an advection–diffusion model". *Bulletin of Volcanology* 74(6), pages 1485–1507. DOI: 10.1007/s00445-012-0609-x.

Lexa, J., J. Šebesta, J. Chavez, W. Hernández, and Z. Pécskay (2011). "Geology and volcanic evolution in the southern part of the San Salvador Metropolitan Area". *Journal of Geosciences*, pages 106–140. DOI: 10.3190/jgeosci.088.

Major, J. J., S. P. Schilling, C. R. Pullinger, C. D. Escobar, C. Chesner, and M. M. Howell (2001). *Lahar-Hazard Zonation for San Miguel Volcano, El Salvador*. Technical report. Open-File Report 01-395.

Mastin, L. G., M. Guffanti, R. Servranckx, P. Webley, S. Barsotti, K. Dean, A. Durant, J. W. Ewert, A. Neri, W. I. Rose, D. Schneider, L. Siebert, B. Stunder, G. Swanson, A. Tupper, A. Volentik, and C. Waythomas (2009). "A multidisciplinary effort to assign realistic source parameters to models of volcanic ash-cloud transport and dispersion during eruptions". *Journal of Volcanology and Geothermal Research* 186(1–2), pages 10–21. DOI: 10.1016/j.jvolgeores.2009.01.008.

Nelder, J. A. and R. Mead (1965). "A Simplex Method for Function Minimization". *The Computer Journal* 7(4), pages 308–313. DOI: 10.1093/comjnl/7.4.308.

Newhall, C. G. and S. Self (1982). "The volcanic explosivity index (VEI) an estimate of explosive magnitude for historical volcanism". *Journal of Geophysical Research* 87(C2), page 1231. DOI: 10.1029/jc087ic02p01231.

Pérez, N. M., P. A. Hernández, E. Padrón, R. Cartagena, R. Olmos, F. Barahona, G. Melián, P. Salazar, and D. L. López (2006). "Anomalous Diffuse CO2 Emission prior to the January 2002 Short-term Unrest at San Miguel Volcano, El Salvador, Central America". *Pure and Applied Geophysics* 163(4), pages 883–896. DOI: 10.1007/s00024-006-0050-1.

Pyle, D. M. (2015). "Sizes of Volcanic Eruptions". In: *The Encyclopedia of Volcanoes*. Edited by H. Sigurdsson. Elsevier, pages 257–264. DOI: 10.1016/b978-0-12-385938-9.00013-4.

Rose, W. I., J. J. Bommer, D. L. López, M. J. Carr, and J. J. Major (2004). *Natural Hazards in El Salvador*. Volume 375. Geological Society of America. ISBN: 9780813723754. DOI: 10.1130/0-8137-2375-2.

Ruth, D. C. and E. S. Calder (2014). "Plate tephra: Preserved bubble walls from large slug bursts during violent Strombolian eruptions". *Geology* 42(1), pages 11–14. DOI: 10.1130/g34859.1.

Scarlato, P., S. Mollo, E. Del Bello, A. von Quadt, R. J. Brown, E. Gutiérrez, B. Martinez-Hackert, and P. Papale (2016). "The 2013 eruption of Chaparrastique volcano (El Salvador): Effects of magma storage, mixing, and decompression". *Chemical Geology* 448, pages 110–122. DOI: 10.1016/j.chemgeo.2016.11.015.

Scollo, S., S. Tarantola, C. Bonadonna, M. Coltelli, and A. Saltelli (2008). "Sensitivity analysis and uncertainty estimation for tephra dispersal models". *Journal of Geophysical Research* 113(B6). DOI: 10.1029/2006jb004864.

Scott, A. C. (2000). "The Pre-Quaternary history of fire". *Palaeogeography, Palaeoclimatology, Palaeoecology* 164(1-4), pages 281–329. DOI: 10.1016/s0031-0182(00)00192-9.

Scott, A. C. and I. J. Glasspool (2005). "Charcoal reflectance as a proxy for the emplacement temperature of pyroclastic flow deposits". *Geology* 33(7), page 589. DOI: 10.1130/g21474.1.

Siebert, L., E. Cottrell, E. Venzke, and B. Andrews (2015). "Earth's Volcanoes and Their Eruptions: An Overview". In: *The Encyclopedia of Volcanoes*. Edited by H. Sigurdsson. Elsevier, pages 239–255. DOI: 10.1016/b978-0-12-385938-9.00012-2.

Sparks, R. S. J., M. I. Bursik, S. N. Carey, J. Gilbert, L. S. Glaze, H. Sigurdsson, and A. W. Woods (1997). *Volcanic plumes*. Wiley, Chichester. ISBN: 0471939013.

Stoiber, R. E. and M. J. Carr (1973). "Quaternary volcanic and tectonic segmentation of Central America". *Bulletin Volcanologique* 37(3), pages 304–325. DOI: 10.1007/bf02597631.

Sun, D., S. Roth, and M. J. Black (2010). "Secrets of optical flow estimation and their principles". *2010 IEEE Computer Society Conference on Computer Vision and Pattern Recognition*. DOI: 10.1109/cvpr.2010.5539939.

– (2014). "A Quantitative Analysis of Current Practices in Optical Flow Estimation and the Principles Behind Them". *International Journal of Computer Vision* 106(2), pages 115–137. DOI: 10.1007/s11263-013-0644-x.

Suwa, H., Y. J. Suzuki, and A. Yokoo (2014). "Estimation of exit velocity of volcanic plume from analysis of vortex structures". *Earth and Planetary Science Letters* 385, pages 154–161. DOI: 10.1016/j.epsl.2013.10.032.

Suzuki, T. (1983). "A theoretical model for dispersion of tephra". In: *Arc volcanism: physics and tectonics*. Edited by D. Shimozuru and I. Yokoyama. Terra Scientific Publishing Company (TERRAPUB) Tokyo, pages 95–113.

Suzuki, Y., A. Costa, and T. Koyaguchi (2016). "On the relationship between eruption intensity and volcanic plume height: Insights from three-dimensional numerical simulations". *Journal of Volcanology and Geothermal Research* 326, pages 120–126. DOI: 10.1016/j.jvolgeores.2016.04.016.

Tournigand, P.-Y., J. Taddeucci, D. Gaudin, J. J. Peña Fernández, E. Del Bello, P. Scarlato, U. Kueppers, J. Sesterhenn, and A. Yokoo (2017). "The Initial Development of Transient Volcanic Plumes as a Function of Source Conditions". *Journal of Geophysical Research: Solid Earth* 122(12), pages 9784–9803. DOI: 10.1002/2017jb014907.

Tsuji, T., M. Ikeda, H. Kishimoto, K. Fujita, N. Nishizaka, and K. Onishi (2017). "Tephra fallout hazard assessment for VEI5 Plinian eruption at Kuju volcano, Japan, using TEPHRA2". In: *IOP Conference Series: Earth and Environmental Science*. Volume 71. 012002. IOP Publishing, pages 1–12. DOI: 10.1088/1755-1315/71/1/012002.

Wadsworth, F. B., E. W. Llewellin, J. I. Farquharson, J. K. Gillies, A. Loisel, L. Frey, E. Ilyinskaya, T. Thordarson, S. Tramontano, E. Lev, M. J. Pankhurst, A. G. Rull, M. Asensio-Ramos, N. M. Pérez, P. A. Hernández, D. Calvo, M. C. Solana, U. Kueppers, and A. P. Santabárbara (2022). "Crowd-sourcing observations of volcanic eruptions during the 2021 Fagradalsfjall and Cumbre Vieja events". *Nature Communications* 13(1). DOI: 10.1038/s41467-022-30333-4.

Webb, E. B., N. R. Varley, D. M. Pyle, and T. A. Mather (2014). "Thermal imaging and analysis of short-lived Vulcanian explosions at Volcán de Colima, Mexico". *Journal of Volcanology and Geothermal Research* 278–279, pages 132–145. DOI: 10.1016/j.jvolgeores.2014.03.013.